

國立台灣大學理學院化學系

碩士論文

Department of Chemistry

College of Science

National Taiwan University

Master's Thesis



氟取代苯並噻二唑型小分子於
有機太陽能電池之合成、性質與應用

Syntheses, Properties, and Applications of Small
Molecules with Fluorinated Benzothiadiazole for Organic
Solar Cells

陳建儒

Chien-Ju Chen

指導教授：汪根權 博士

Advisor: Ken-Tsung Wong, Ph.D.

中華民國 104 年 7 月

July 2015



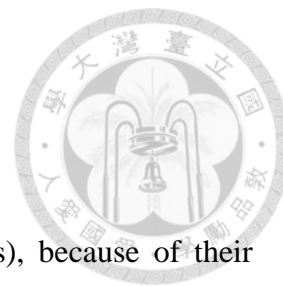


中文摘要

小分子太陽能電池因具有分子結構明確、每批品質較一致之優勢，故近年吸引相當多領域投入研究。

先前的文獻指出，在電子予體中引入氟原子，可以同時降低分子的最高占有分子軌域與最低未占有分子軌域之能階。而降低之能階有助於太陽能電池獲得較高之開路電壓。故在本篇論文中，我們設計並合成了具予體-受體-受體 (D-A-A) 架構之含氟電子予體。其分別以噻吩與苯環為架橋，並在苯並噻二唑上引入朝內或朝外之氟原子，可得 **DTCTiFBT**，**DTCToFBT**，**DTCPiFBT** 及 **DTCPoFBT**。四個分子的最大吸收波長在 500-600 nm，且有良好的吸收效率。相較於其對照組，四個分子皆表現些微紅移之吸收光譜，以及較低之能階。將其與電子受體材料 C₆₀ 共蒸鍍，並調變適當的膜厚及混合比例製作太陽能電池元件。四個分子之表現皆較未引入氟的對照電子予體優異。在與 C₆₀ 共蒸鍍的元件中，以噻吩為架橋的 **DTCToFBT/C₆₀** 最佳化元件結構可得到 0.83 V 之開路電壓，6.85 mA/cm² 之短路電流，以及 3.28% 之光電轉換效率。而以苯環為架橋的 **DTCPoFBT** 最佳化元件結構可得到 0.88 V 之開路電壓，6.50 mA/cm² 之短路電流，以及 3.62% 之光電轉換效率。本論文展示了 D-A-A 架構之含氟電子予體之結構與性質對應。

Abstract



In recent years, small-molecule organic solar cells (SMOSCs), because of their well-defined structure and batch-to-batch reproducibility, are under intense investigations.

We anticipate that the introduction of fluorine atom onto a donor molecule can lower the highest occupied molecular orbital (HOMO) and lowest unoccupied molecular orbital (LUMO) of the donor, giving the SMOSC device a larger open circuit voltage (V_{oc}). In this thesis, four molecules configured as donor-acceptor-acceptor (D-A-A) were synthesized and characterized. Two electron donating moieties, namely ditolyaminothiophene or ditolyaminophenylene were respectively connected to an electron deficient cyano group, via F-substituted [2,1,3]benzothiadiazole (**FBT**) to give **DTCTiFBT**, **DTCToFBT**, **DTCPiFBT**, and **DTCPoFBT**. Four molecules showed slightly red-shifted absorption and lowered HOMO and LUMO level as compared to those of the non-fluorinated counterparts. After fabrication with fullerene C_{60} as the active layers in SMOSCs, all molecules showed better performance compared to the non-fluorinated counterparts. Among all, thiophene-bridged **DTCToFBT**/ C_{60} device exhibited a V_{oc} of 0.83 V, a short circuit current density (J_{sc}) of 6.85 mA/cm², and a fill factor (FF) of 0.58, achieving a power conversion efficiency (PCE) of 3.28%. Phenylene-bridged **DTCPoFBT**/ C_{60} device exhibited a V_{oc} of 0.88 V, a J_{sc} of 6.50 mA/cm², and a FF of 0.63, achieving a PCE of 3.62%. A clear structure-property relationship has been established.



Contents

中文摘要	i
Abstract.....	ii
Index of Figure	iv
Index of Table	v
Index of Scheme	vi
Chemical Structure Index	vii
Chapter 1 Introduction.....	1
Chapter 2 DTCTiFBT and DTCToFBT.....	11
2-1 Syntheses.....	11
2-2 Optical Properties.....	12
2-3 Electrochemical Properties.....	13
2-4 Theoretical Calculations.....	14
2-5 Crystal Structures and Packings.....	17
2-6 Thermal Properties	18
2-7 Photovoltaic and Electrochemical Impedance Characteristics.....	19
Chapter 3 DTCPiFBT and DTCPoFBT.....	21
3-1 Syntheses.....	21
3-2 Optical Properties.....	21
3-3 Electrochemical Properties.....	23
3-4 Theoretical Calculations.....	23
3-5 Crystal Structures and Packings.....	26
3-6 Thermal Properties	27
3-7 Photovoltaic and Electrochemical Impedance Characteristics.....	28
Conclusions	30
Experiment Session	31
Syntheses and Materials.	31
General Experiment.....	37
References	40
Appendix A ^1H and ^{13}C NMR Spectra	43
Appendix B TGA and DSC Thermogram	51
Appendix C X-ray Crystallography Data	56

Index of Figure



Figure 1-1. The spectrum of solar radiation at Earth's surface.	2
Figure 1-2. Aromatic and quinoid resonance forms for some conjugated polymers and their relative population in ground state.....	4
Figure 2-1. Absorption spectra of DTCTiFBT (triangles) and DTCToFBT (diamonds) in (a) CH ₂ Cl ₂ solutions and (b) vacuum deposited thin films.....	12
Figure 2-2. Cyclic voltammograms of DTCTiFBT and DTCToFBT	13
Figure 2-3. DFT-optimized geometries for DTCTiFBT and DTCToFBT	15
Figure 2-4. Isodensity surface plots of the HOMO (green) and LUMO (red) of DTCTiFBT and DTCToFBT	17
Figure 2-5. Crystal structures of DTCTiFBT in molecular packing.	18
Figure 2-6. (a) J-V curves and (b) EQE spectra for DTCTiFBT (triangles), DTCToFBT (diamonds), and DTCTB (pentagons) for C ₆₀ -based OPV.....	20
Figure 3-1. Absorption spectra of DTCPiFBT (square) and DTCPoFBT (circle) in (a) CH ₂ Cl ₂ solutions and (b) vacuum deposited thin films.	22
Figure 3-2. Cyclic voltammograms of DTCPiFBT and DTCPoFBT	23
Figure 3-3. DFT-optimized geometries for DTCPiFBT and DTCPoFBT	24
Figure 3-4. Isodensity surface plots of the HOMO (green) and LUMO (red) of DTCPiFBT and DTCPoFBT	26
Figure 3-5. Crystal structures of DTCPiFBT and DTCPoFBT in molecular packing.	27
Figure 3-6. (a) J-V curves and (b) EQE spectra for DTCPiFBT (square), and DTCPoFBT (circle) for C ₆₀ -based OPV.....	29

Index of Table



Table 1-1. Electrochemical parameters and device performance of several fluorinated electron donors.	8
Table 2-1. Photophysical and electrochemical parameters for DTCTiFBT , DTCToFBT , and DTCTB	13
Table 2-2. Dipole moment parameters for DTCTiFBT , DTCToFBT , and DTCTB	16
Table 2-3. TD-DFT calculated oscillator strengths, absorption wavelengths, molecular orbital compositions, and transition characters for DTCTiFBT and DTCToFBT	16
Table 2-4. Thermal parameters for DTCTiFBT , DTCToFBT , and DTCTB	19
Table 2-5. Photovoltaic parameters for DTCTiFBT , DTCToFBT , and DTCTB with OPV structure: ITO / MoO ₃ / dye: C ₆₀ (x nm) / C ₆₀ (y nm) / BCP / Al. .	20
Table 3-1. Photophysical and electrochemical parameters for DTCPiFBT , DTCPoFBT , and DTCPB	22
Table 3-2. Dipole moment parameters for DTCPiFBT , DTCTPoFBT , and DTCPB	25
Table 3-3. TD-DFT calculated oscillator strengths, absorption wavelengths, molecular orbital compositions, and transition characters for DTCPiFBT and DTCPoFBT	25
Table 3-4. Thermal parameters for DTCPiFBT , DTCPoFBT , and DTCPB	28
Table 3-5. Photovoltaic parameters for DTCPiFBT and DTCPoFBT with OPV structure: ITO / MoO ₃ / dye: C ₆₀ (x nm) / BCP / Al.	29

Index of Scheme

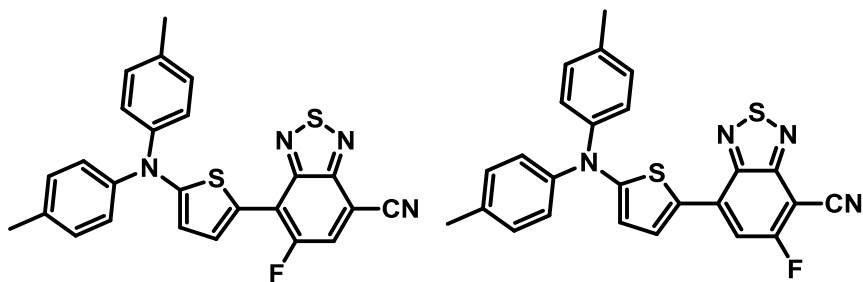


Scheme 1-1. Small molecule electron donors for OSCs achieving PCE over 8%..	5
Scheme 1-2. Fluorinated electron donors for OSCs achieving PCE over 6%.	6
Scheme 1-3. Chemical structures of several fluorinated electron donors.	7
Scheme 1-4. Chemical structures and performance of DTCTB and DTCPB	9
Scheme 1-5. Four D-A-A electron donors synthesized and characterized in this thesis.....	10
Scheme 2-1. Synthetic route for FBTCN , DTCTiFBT , and DTCToFBT	11
Scheme 3-1. Synthetic route for DTCPiFBT and DTCPoFBT	21

Chemical Structure Index

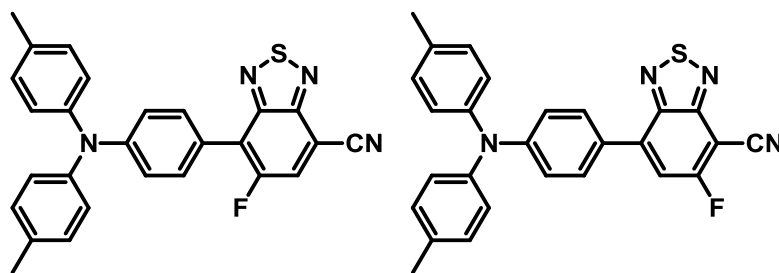


Target Compounds



DTCTiFBT

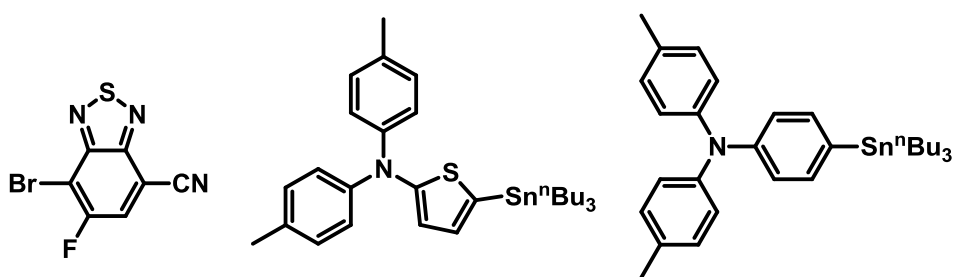
DTCToFBT



DTCPiFBT

DTCPoFBT

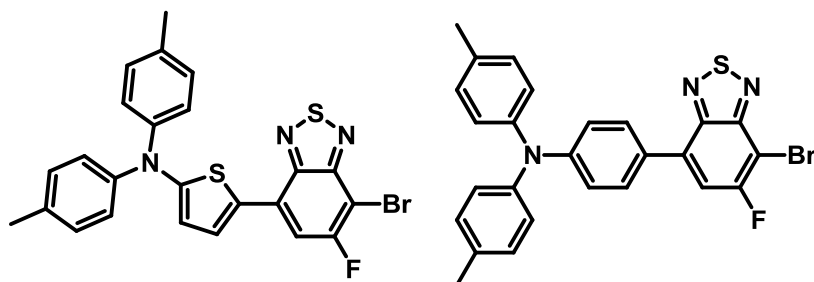
Intermediates



FBTCN

dtat-tin

dtap-tin



DTTToFBTBr

DTPoFBTBr



Chapter 1 Introduction



Energy issue has raised increasing attention over the past decades. Since fossil fuels are expected to be used up within 21th century, several types of alternative energy, including solar energy, biofuel, wind power, tidal power, and geothermal energy, are currently under intensive investigation. It is beautiful to extract electricity directly from the sun, which is clean, safe, and crucial for our lives. Thus, different kinds of photovoltaic devices (PVs) have emerged and become a prominent subject in the past few decades.¹ Silicon-based solar cells, because of their well-studied properties, long stability, and high power conversion efficiency (PCE), have been widely used for generating electricity. Despite several advantages of silicon-based solar cells, there are some drawbacks, like high production cost and related environment impact, which have impelled us to develop new types of PVs continuously.¹ Among all, organic solar cells (OSCs) are one of the possible solutions.

The fascinating features of OSCs are the potential of large-area and roll-to-roll fabrication, light-weight and flexible devices, lower cost, and low impact to environment. Nowadays, different kinds of OSCs have been investigated. The best-known designs of device are dye-sensitized solar cells (DSSCs) and organic thin-film solar cells. DSSCs have been well studied and the maxima PCEs are steadily over 10%.² Organic thin-film solar cells comprise an electron acceptor, which is usually fullerene derivatives, and an organic electron donor. When an electron donor absorbs a photon, an electron in the highest occupied molecular orbital (HOMO) is excited to the lowest unoccupied molecular orbital (LUMO). The photogenerated exciton diffuses within the electron donor towards the interface to the electron acceptor. If the energy level difference between the electron donor and the electron

acceptor is larger than the exciton binding energy, usually 0.3–1.0 eV,³ charge transfer from the donor molecule to the acceptor molecule occurs. The electron is transferred to the acceptor molecule via the energetically favorable driving force, resulting in a polaron pair. After dissociation, the hole stays and transports on the electron donor, which is thus called p-type material, whereas the electron travels on the electron acceptor, thus called n-type material. The polarons can transport to electrodes and deliver photocurrent. The donor-acceptor heterojunction plays an important role in device performance. Since the diffusion length of excitons in organic electronic materials is typically within 20 nm,⁴ large interface area is essential for the excitons to reach the heterojunction interface. In bulk heterojunction cells (BHJ), an electron donor and an electron acceptor are cast simultaneously. Hence, two components are allowed to interpenetrate, creating huge extension of interface area. Consequently, BHJ is the most widely used architecture for organic thin-film solar cells.³⁻⁴

An electron donor should capture photons from solar radiation efficiently to provide high photocurrent. The most intense irradiance region of solar spans 400–700 nm at Earth's surface (Figure 1-1).⁵ To gain power conversion efficiency, the optical absorption of an electron donor should span visible range and extend to near-infrared region. Luckily, powerful synthetic methods have been developed to invent electron donors with appropriate properties.

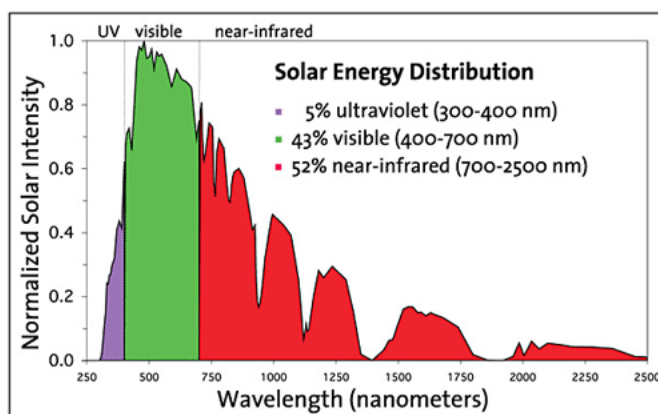
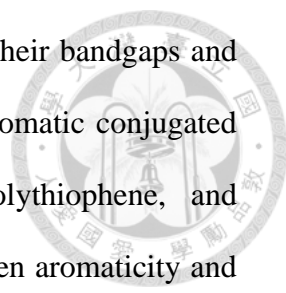


Figure 1-1. The spectrum of solar radiation at Earth's surface.



Judicious design of electron donors is crucial for controlling their bandgaps and thus utilizing solar radiation. As shown in Figure 1-2, four polyaromatic conjugated polymers, namely polyphenylene, poly(phenylenevinylene), polythiophene, and polyisothianaphthene, are chosen to illustrate the relationship between aromaticity and bandgap.⁶ In ground state, all polymers exhibit two forms with nondegenerate energy: aromatic and quinoid form. In aromatic form, the π -electrons are confined in each ring to gain resonance stabilized energy, resulting in extra stability. In quinoid form, however, the π -electrons are delocalized and the aromaticity is destroyed, which is thus energetically less stable than aromatic form. Consequently, there is more population in aromatic form for the first three polymers. The large bandgap (3.2 eV) of polyphenylene results from the high resonance stabilized energy of benzene (36 kcal mol⁻¹), whereas the relatively low aromaticity of thiophene (29 kcal mol⁻¹)⁷ gives a small bandgap (2.0 eV) for polythiophene. For poly(phenylenevinylene), insertion of double bonds can dilute the overall aromaticity and thus reduce the bandgap (2.5 eV). To increase the quinoid population effectively, fused rings are adopted to maintain the aromaticity in quinoid form. The higher resonance stabilized energy of benzene than thiophene lets polyisothianaphthene tend to favor quinoid form to keep the aromaticity of benzene. To sum up, higher aromaticity components result in larger bandgap; however, the aromaticity can be utilized in fused rings to increase the quinoid population. In this thesis, an electron-withdrawing [2,1,3]benzothiadiazole moiety with high quinoidal character was utilized in conjugated backbone to facilitate π -electron delocalization.⁸

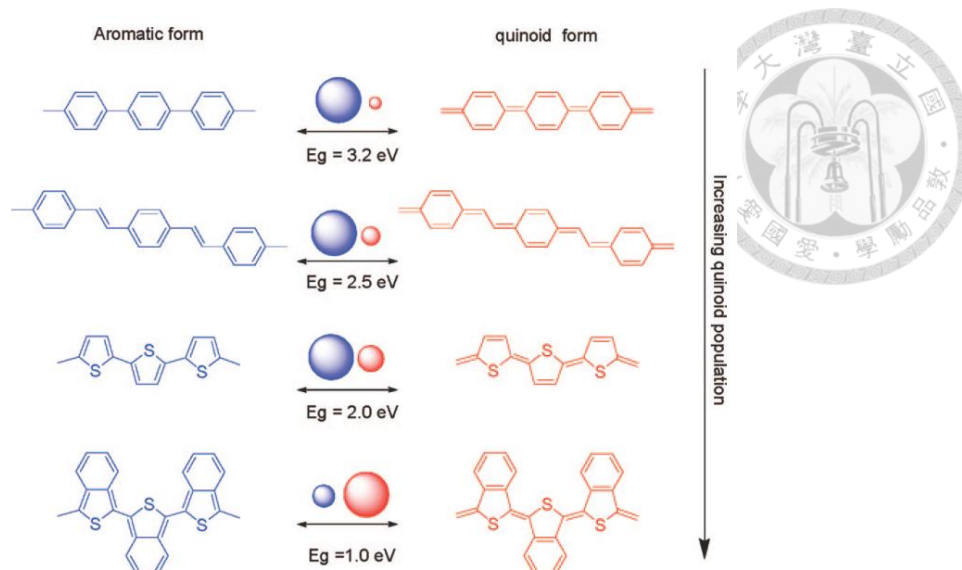
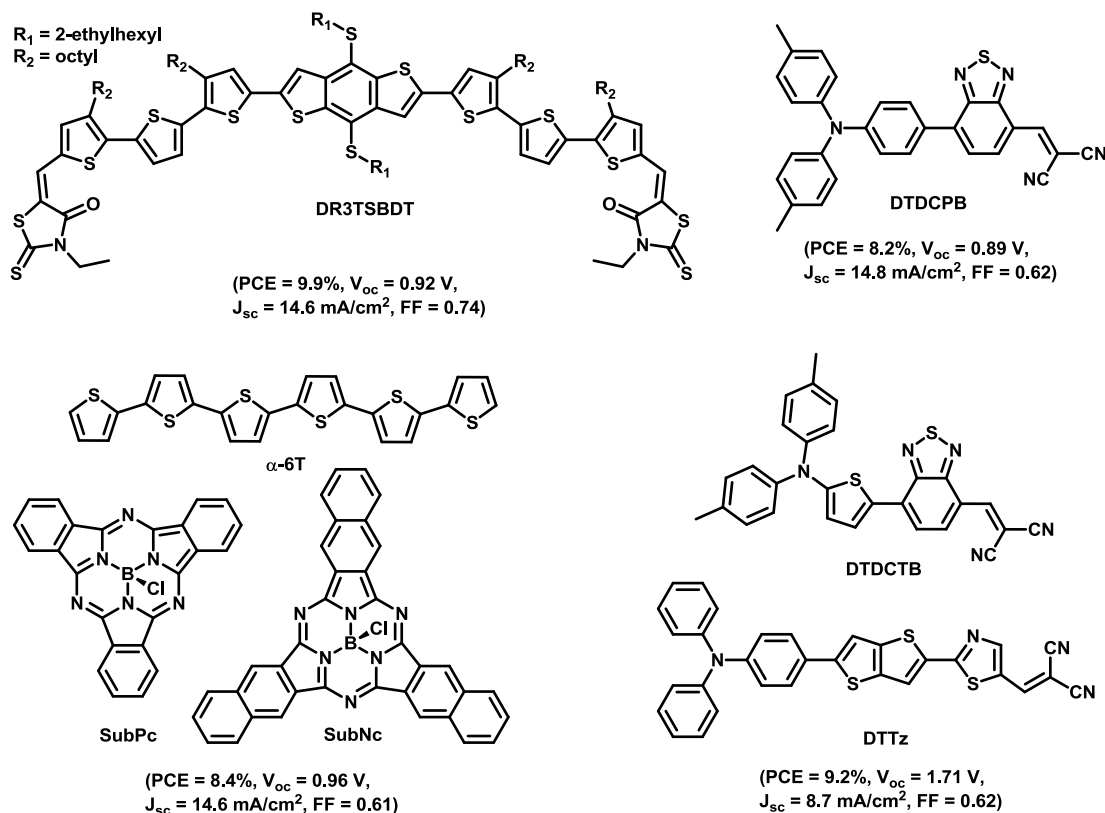


Figure 1-2. Aromatic and quinoid resonance forms for some conjugated polymers and their relative population in ground state.

After fabrication into photovoltaic devices, there are three key parameters to determine the power conversion efficiency of a PV: the open-circuit voltage (V_{oc}), short-circuit current density (J_{sc}), and fill factor (FF). The fill factor is defined as the following equation: $FF = \frac{V_{MPP} * J_{MPP}}{V_{oc} * J_{sc}}$, where MPP is the abbreviation of the maximum power point. As a result, power conversion efficiency can be written as follows: $PCE = \frac{V_{oc} * J_{sc} * FF}{P_{in}}$, where P_{in} denotes the input power. In order to obtain high J_{sc} , PV devices should possess large shunt resistance (R_{sh}) and small series resistance (R_s).⁹ On the other hand, since V_{oc} is mainly determined by the energy difference between the HOMO of an electron donor and the LUMO of an electron acceptor,¹⁰ lower HOMO of an electron donor may realize higher V_{oc} . FF implies morphology in the active layer, and the possibility the photogenerated carriers can be extracted.

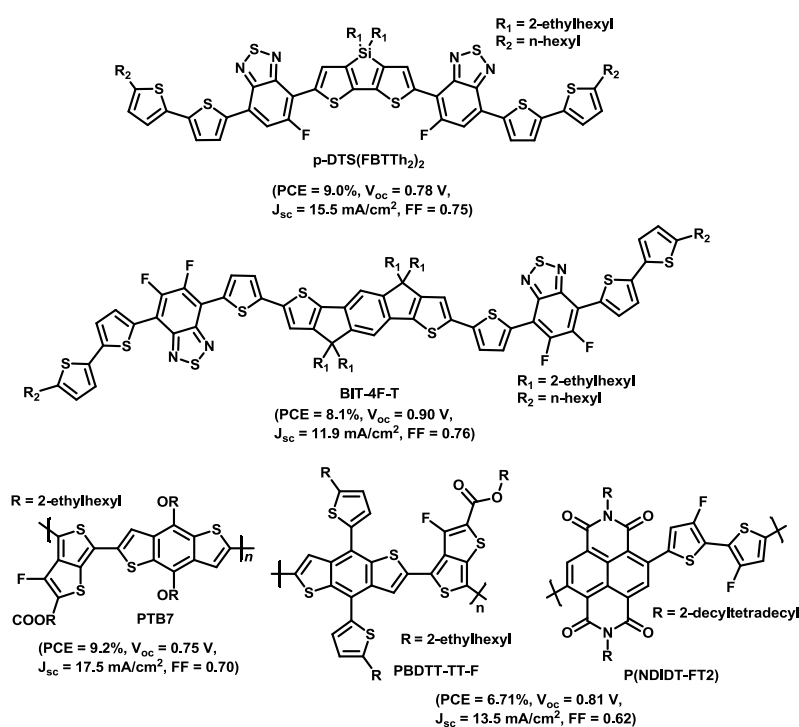
In bulk heterojunction cells, electron donors can be roughly classified into two categories: small molecule and polymer. Small molecule organic solar cells

(SMOSCs), because of their well-defined structure and batch-to-batch reproducibility compared to polymer solar cells (PSCs), are attracting more attention. Several small molecules were employed as electron donors and achieved PCE over 8% (Scheme 1-1). **DR3TSBDT**, featuring benzodithiophene (BDT) as the electron-donating unit for solution-processed BHJ, showed a certified PCE of 9.9%.¹¹ From our previous research, vacuum-deposited **DTDCPB** solar cell performed a maximum PCE of 8.2%, which is one of the highest PCE reported for asymmetric dipolar electron donors.¹² A cascade architecture non-fullerene OSC comprising an electron donor α -**6T** and two electron acceptors, **SubPc** and **SubNc**, reached a remarkable PCE of 8.4%.¹³ Furthermore, a tandem OSC comprising **DTTz** for visible absorption and **DTDCTB** for near-infrared absorption could achieve a high PCE of 9.2%.¹⁴ Such results indicate that SMOSCs can yield high PCE and are worth further investigation.



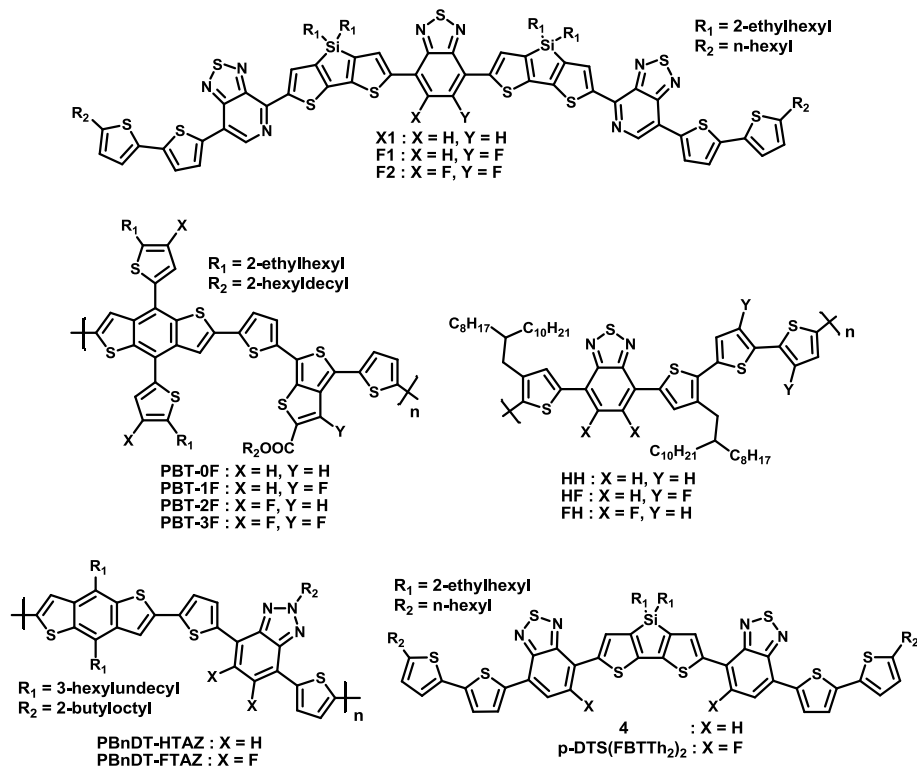
Scheme 1-1. Small molecule electron donors for OSCs achieving PCE over 8%.

Recently, there are extensive studies of the introduction of heteroatoms on electron donors, one of which is a fluorine atom. Some representative chemical structures and device performance of fluorinated electron donors are shown in Scheme 1-2. Dithienosilole (DTS) centered **p-DTS(FBTTh₂)₂**,¹⁵ connecting with fluorobenzothiadiazole (FBT) as electron withdrawing group (EWG), performed a maximum PCE of 9.0%,¹⁶ which is prominently higher than the PCE 0.2% of the non-fluorinated counterpart **4**.¹⁷ **BIT-4F-T**, comprising difluorobenzothiadiazole (dFBT) as EWG, delivered a maximum PCE of 8.1%.¹⁸ Polymer BHJ utilizing **PTB7** as an electron donor, which features a fluorinated-thienothiophene moiety, could obtain an impressive PCE of 9.2%.¹⁹ All-polymer BHJ, utilizing both fluorinated electron donor **PBDTT-TT-F** and electron acceptor **P(NDIDT-FT2)**, yielded a maximum PCE of 6.7%,²⁰ which is among the highest PCE reported all-polymer solar cells. Based on these investigations, fluorinated EWGs are promising components to access high power conversion efficiency for OSCs.



Scheme 1-2. Fluorinated electron donors for OSCs achieving PCE over 6%.

Many studies revealed the relationship between fluorination and energy level. Some representative series of fluorinated electron donors are illustrated in Scheme 1-3 and summarized in Table 1-1. As the introduction of fluorine atom(s), both HOMO and LUMO energy levels were lowered for all electron donors in three conditions: (1) the decrement of HOMO is larger than that of LUMO, resulting in larger bandgap, like **X1** series²¹ and **PBT-0F** series.²² (2) The decrement of HOMO is equal to that of LUMO, resulting in equal bandgap, like **HH** series²³ and **p-DTS(FBTTh₂)₂** series.^{15, 17} (3) The decrement of HOMO is smaller than that of LUMO, resulting in smaller bandgap, like **PBnDT-HTAZ** series.²⁴ In all conditions, the lowered HOMO can contribute to high V_{oc} . Furthermore, in the third condition, smaller bandgap may lead to bathochromic absorption, which is beneficial for pursuing higher J_{sc} . However, the third condition is generally less reported.



Scheme 1-3. Chemical structures of several fluorinated electron donors.

Table 1-1. Electrochemical parameters and device performance of several fluorinated electron donors.

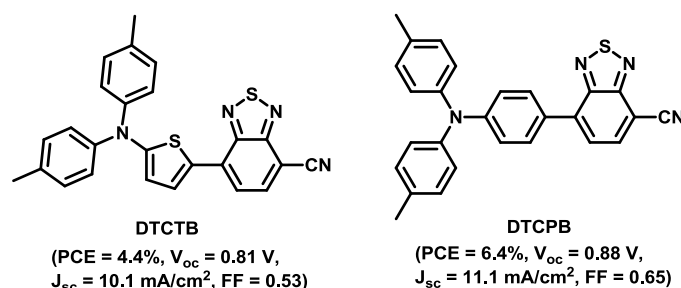
	HOMO (eV) ^a	LUMO (eV)	bandgap (eV) ^c	V _{oc} (V)	PCE (%)
X1	-5.17	-3.73 ^a	1.44	0.71	5.8
F1	-5.20	-3.73 ^a	1.47	0.75	6.3
F2	-5.26	-3.75 ^a	1.51	0.76	6.1
PBT-0F	-4.90	-3.10 ^a	1.80	0.56	4.5
PBT-1F	-4.95	-3.12 ^a	1.83	0.60	5.6
PBT-2F	-5.15	-3.27 ^a	1.88	0.74	7.2
PBT-3F	-5.20	-3.30 ^a	1.90	0.78	8.6
HH	-5.31	-3.73 ^b	1.58	0.73	1.6
HF	-5.42	-3.84 ^b	1.58	0.78	7.1
FH	-5.38	-3.80 ^b	1.58	0.72	6.4
4	-5.08	-3.30 ^a	1.78	0.70-0.83	0.2
p-DTS(FBTTh₂)₂	-5.12	-3.34 ^a	1.78	0.81	7.0
PBnDT-HTAZ	-5.29	-2.87 ^a	2.42	0.70	4.3
PBnDT-FTAZ	-5.36	-3.05 ^a	2.31	0.79	6.8

^a calculated from the cyclic voltammogram. ^b optical bandgap + HOMO. ^c LUMO – HOMO.

Though there is a clear relationship between fluorination and the decrement of both HOMO and LUMO, such conclusion is typically based on polymers. There are fewer literatures about small molecules. Most of them are based on centrosymmetric configurations, e.g. D₂-A₁-D₁-A₁-D₂ or D₂-A₂-D₁-A₁-D₁-A₂-D₂ architecture. Research based on asymmetric configuration, such as D-A-A type, is relatively rare. This thesis provided examples for the second and the third condition based on D-A-A small molecules.

From our previous study of electron donors for SMOSCs, **DTCTB** and **DTCPB**, in which two electron-donating ditolylaminophenyl and ditolylaminothienyl moieties were respectively connected to an electron-withdrawing cyano group through another

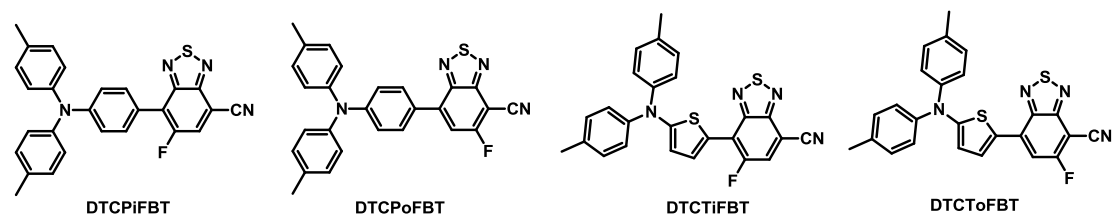
electron-withdrawing [2,1,3]benzothiadiazole moiety, performed a maximum PCE of 4.4% and 6.4% on C₇₀-based devices (Scheme 1-4). It is noteworthy that the fill factor is very high, especially for **DTCPB** (FF = 0.65). Organic photovoltaic (OPV) devices with high FF have a high R_{sh} and a low R_s, suggesting the morphology after blended with fullerenes is very beneficial for reducing the internal loss of current produced by the devices. Encouraged by the promising results, we decide to introduce a fluorine atom onto BT moieties of **DTCTB** and **DTCPB** as a pendant group to alter energy levels. Since the atomic weight is 19 Da for a fluorine atom, the change of molecular weight (MW) is small for a D-A-A molecule with MW 400–500 Da. We expect that replacing a hydrogen atom with a fluorine atom will make little change to the benign morphology while providing additional interactions or steric hindrance.



Scheme 1-4. Chemical structures and performance of **DTCTB** and **DTCPB**.

In this thesis, four donor-acceptor-acceptor (D-A-A) structured electron donors were synthesized and characterized, namely **DTCTiFBT**, **DTCToFBT**, **DTCPiFBT**, and **DTCPoFBT** (Scheme 1-5). The difference in aromaticity of benzene and thiophene along with the different position of the inserted fluorine atom can lead to different performances and meaningful discussions. Their corresponding BHJ devices and solid film properties were fabricated and measured by Prof. Jiun-Haw Lee and Mr. Yi-Ze Hsiao at the Graduate Institute of Photonics and Optoelectronics, National Taiwan University. For comparison, this thesis also included the non-fluorinated

counterparts, **DTCTB** and **DTCPB**, synthesized and characterized by Dr. Hao-Chun Ting and Mr. Chia-Hsun Chen. The density functional theory (DFT) and time-dependent density functional theory (TD-DFT) theoretical calculations of six molecules were performed at CAM-B3LYP/6-311G(d,p) level by Dr. Shu-Hua Chou.



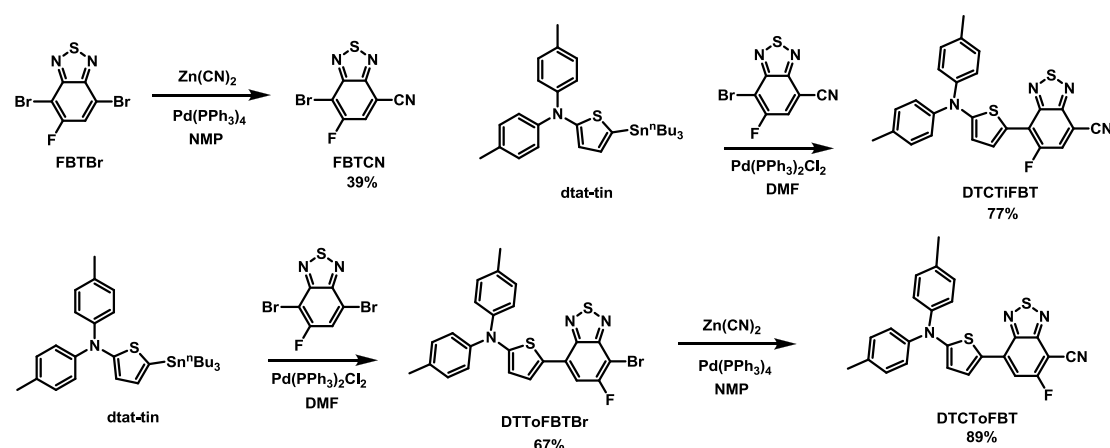
Scheme 1-5. Four D-A-A electron donors synthesized and characterized in this thesis.

Chapter 2 DTCTiFBT and DTCToFBT



2-1 Syntheses

The synthetic route of **FBTCN**, **DTCTiFBT**, and **DTCToFBT** is illustrated in Scheme 2-1. **FBTBr** was adopted as the starting material and synthesized according to the previous literature¹⁵. **FBTBr** underwent Palladium-catalyzed cyanation to give the key intermediate **FBTCN** in 39% yield. Stille coupling of 4-(*N,N*-ditolylamino)-1-(tri-*n*-butylstannyl)thiophene (**dtat-tin**) and **FBTCN** afforded **DTCTiFBT** in 77% yield. For **DTCToFBT**, **dtat-tin** was reacted with **FBTBr** via Stille coupling to afford **DTToFBTBr** in 67% yield, which subsequently underwent Palladium-catalyzed cyanation to give **DTCToFBT** in 89% yield. From infrared (IR) spectra analyses, **DTCTiFBT** and **DTCToFBT** exhibit distinct absorption of nitrile group in 2222 and 2227 cm^{-1} respectively, while **DTToFBTBr** shows no absorption in 2210–2260 cm^{-1} .²⁵ Their chemical structures were further confirmed via nuclear magnetic resonance spectroscopy (NMR) and mass spectroscopy.



Scheme 2-1. Synthetic route for **FBTCN**, **DTCTiFBT**, and **DTCToFBT**.

2-2 Optical Properties

Optical properties of **DTCTiFBT** and **DTCToFBT** are shown in Figure 2-1. Their corresponding properties are summarized in Table 2-1. In solution, both molecules show slightly bathochromic shifts in absorption compared to **DTCTB** due to the introduction of a fluorine atom. All molecules perform most intensive absorption band located in 500–700 nm and extinction coefficient around 23000 $M^{-1}cm^{-1}$, which could be attributed to charge transfer transition from the electron-donating amine moieties to the electron withdrawing benzothiadiazole moieties. In vacuum deposited thin films, all molecules exhibit further bathochromic shifts in their absorption maxima in the same trend as solution state.

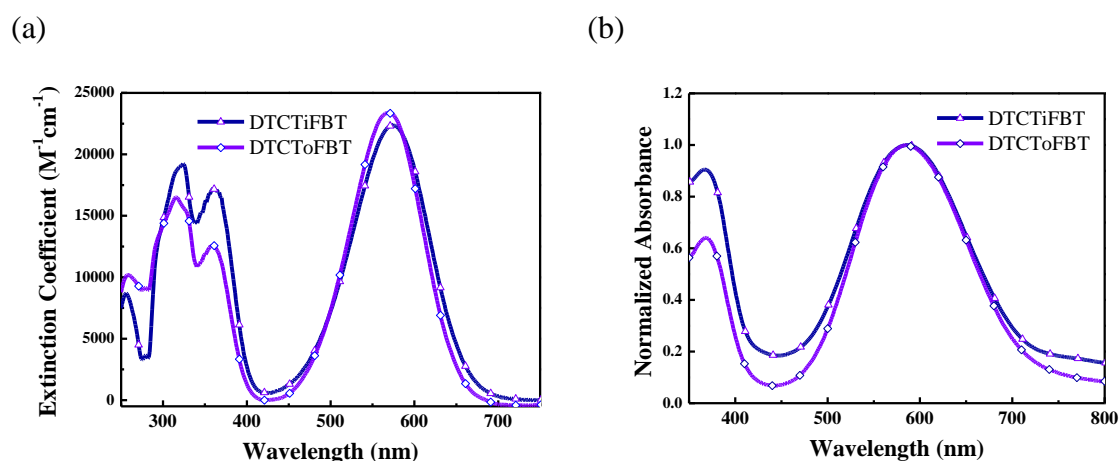


Figure 2-1. Absorption spectra of **DTCTiFBT** (triangles) and **DTCToFBT** (diamonds) in (a) CH_2Cl_2 solutions and (b) vacuum deposited thin films.

Table 2-1. Photophysical and electrochemical parameters for **DTCTiFBT**, **DTCToFBT**, and **DTCTB**.

dyes	λ_{\max} soln (nm) (ϵ , $M^{-1} \text{ cm}^{-1}$)	λ_{\max} film (nm)	HOMO ^a (CV)(eV)	LUMO ^a (CV)(eV)	E_g^{CV} (eV)	IP ^b (eV)
DTCTiFBT	574 (22400)	586	-5.49	-3.66	1.83	5.43
DTCToFBT	569 (23400)	585	-5.49	-3.66	1.83	5.44
DTCTB ²⁶	563 (23200)	574	-5.46	-3.60	1.86	5.40

^a HOMO (eV) = e [-5.1 - (E_{ox} - E_{Fc/Fc⁺})] & LUMO (eV) = e [-5.1 - (E_{red} - E_{Fc/Fc⁺})]. ^b

Determined by photoelectron spectrometer AC-2.

2-3 Electrochemical Properties

Cyclic voltammograms of **DTCTiFBT** and **DTCToFBT** are shown in Figure 2-2. Both molecules exhibit same oxidation and reduction potential in solution state. The energy level of HOMO is -5.49 eV and the energy level of LUMO is -3.66 eV, which are both lower than those of **DTCTB**. Moreover, the LUMO energy level is lowered more than the HOMO energy level, resulting in slightly narrowed energy bandgap. The lowered HOMO and the bathochromic absorption are beneficial for pursuing high V_{oc} and J_{sc} respectively, which showed our molecular design is promising for efficient OPV devices.

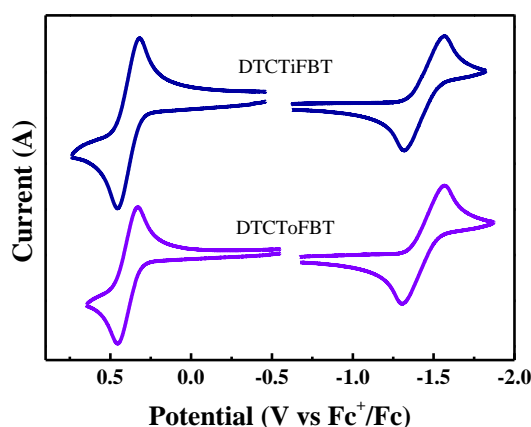
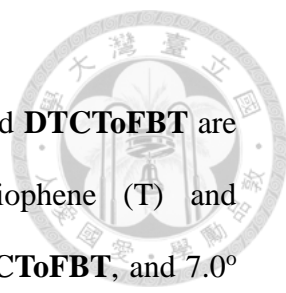


Figure 2-2. Cyclic voltammograms of **DTCTiFBT** and **DTCToFBT**.

2-4 Theoretical Calculations



DFT calculations of optimized geometries for **DTCTiFBT** and **DTCToFBT** are illustrated in Figure 2-3. The dihedral angles between thiophene (T) and benzothiadiazole (BT) units are 3.5° for **DTCTiFBT**, 4.2° for **DTCToFBT**, and 7.0° for **DTCTB**. The coplanarity of these molecules is presumably due to van der Waals (vdW) forces between the inward hydrogen atom on BT unit and the sulfur atom on T unit, as well as between the inward nitrogen atom on BT unit and the outward hydrogen atom on T unit. The coplanarity of **DTCTiFBT** is more strengthened due to the substitution of inward electron-deficient fluorine atom, and thus the stronger interaction with the electron-rich sulfur atom. The speculation was confirmed by calculating the distance between the atoms fore-mentioned via space-filling model, which reveals contact between those atoms mentioned. Such coplanarity enhances effective conjugation length and facilitates the intramolecular charge transfer from the electron donating group to the electron withdrawing group, resulting in bathochromic shift and high extinction coefficient. The coplanarity also provides benign intermolecular π - π interaction, which is beneficial for close packing in solid film.

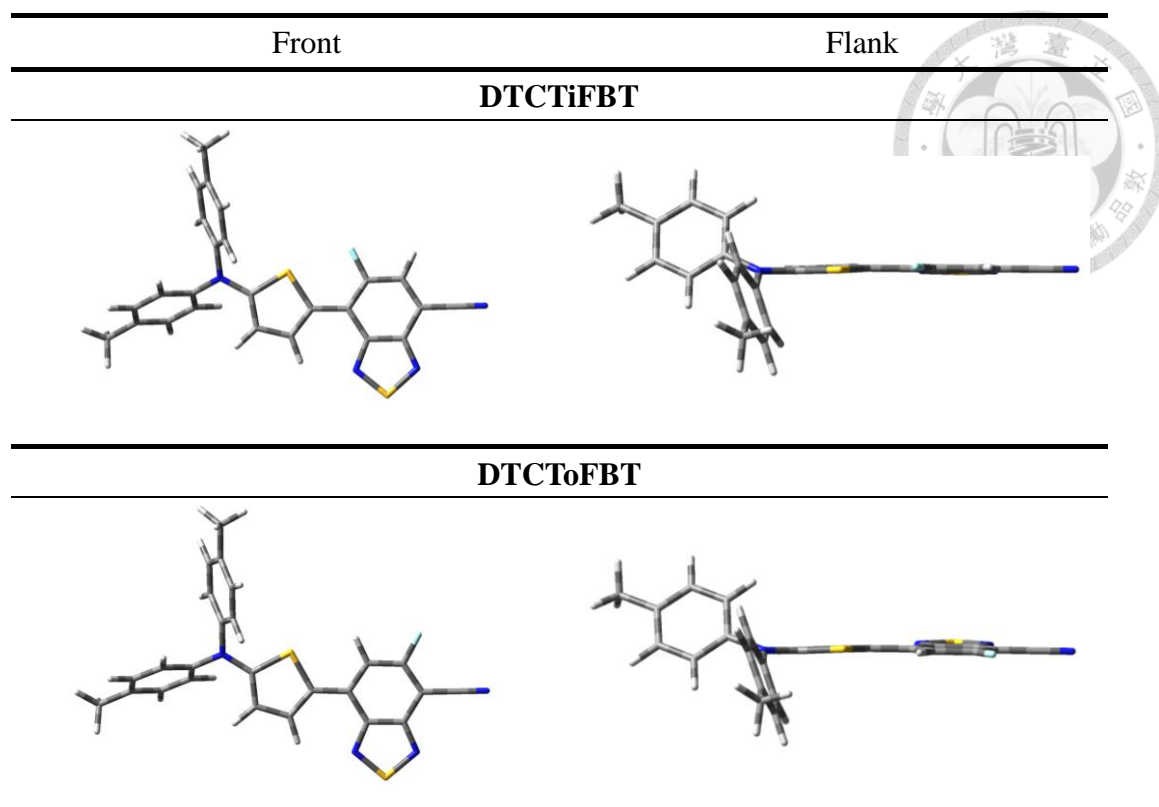


Figure 2-3. DFT-optimized geometries for **DTCTiFBT** and **DTCToFBT**.

The dipole moments of **DTCTiFBT**, **DTCToFBT**, and **DTCTB** are summarized in Table 2-2. The dipole moment for all six dyes in this thesis point from electron donating amines toward electron withdrawing BT and cyano groups. As compared to **DTCTB**, **DTCTiFBT** shows a smaller dipole moment at the ground state, which is cancelled out by the inward direction of the fluorine atom. However, the outward fluorine atom on **DTCToFBT** lines same direction with the molecular dipole moment, resulting in an increment. At the first excited state (S_1), because of further charge separation caused by charge transfer, all molecules show larger dipole moment in same trend, giving a positive $\Delta\mu_{ge}$. For the overall dipole moment overlap between S_0 and S_1 , since μ_g and μ_e point to nearly the same direction, μ_{tr} is very close to μ_g for each molecule. We anticipate that a higher μ_e is beneficial for charge separation and thus the incident photo-to-light conversion efficiency.

Table 2-2. Dipole moment parameters for **DTCTiFBT**, **DTCToFBT**, and **DTCTB**.

dyes	μ_g^a (D)	μ_e^b (D)	$\Delta\mu_{ge}^c$ (D)	μ_{tr}^d (D)
DTCTiFBT	9.68	13.08	5.60	9.46
DTCToFBT	13.28	16.14	3.67	13.24
DTCTB	11.21	14.64	4.51	11.14

^a μ_g : total dipole moment at the ground state (S_0). ^b μ_e : total dipole moment at the first excited state (S_1). ^c $\Delta\mu_{ge}$: overall dipole moment change between S_0 and S_1 . ^d μ_{tr} : overall dipole moment overlap between S_0 and S_1 .

Table 2-3. TD-DFT calculated oscillator strengths, absorption wavelengths, molecular orbital compositions, and transition characters for **DTCTiFBT** and **DTCToFBT**.

dyes	electronic transition, f	$\lambda_{exp} / \lambda_{calc}$ (nm)	MO Composition	character
DTCTiFBT	$S_0 \rightarrow S_1$, 0.7495	574/496	5% HOMO -1 \rightarrow LUMO 92% HOMO \rightarrow LUMO	CT
DTCToFBT	$S_0 \rightarrow S_1$, 0.8416	569/489	4% HOMO -1 \rightarrow LUMO 92% HOMO \rightarrow LUMO	CT

Since the fact that (1) the charge transfer intensity of **DTCTiFBT** and **DTCToFBT** are higher than $\pi-\pi^*$ band in intensity theoretically and experimentally, and (2) the main transition of both molecules are from HOMO to LUMO (Table 2-3), we selectively reported isodensity surface plots of the HOMOs and LUMOs of both molecules. As shown in Figure 2-4, the HOMOs of the molecules are mainly populated at ditolylamine and thiophene fragments, whereas the LUMOs are mainly localized at benzothiadiazole and cyano units. The benign separation between HOMO and LUMO facilitates charge transfer absorption, which is beneficial for utilizing the most intense solar irradiance region.

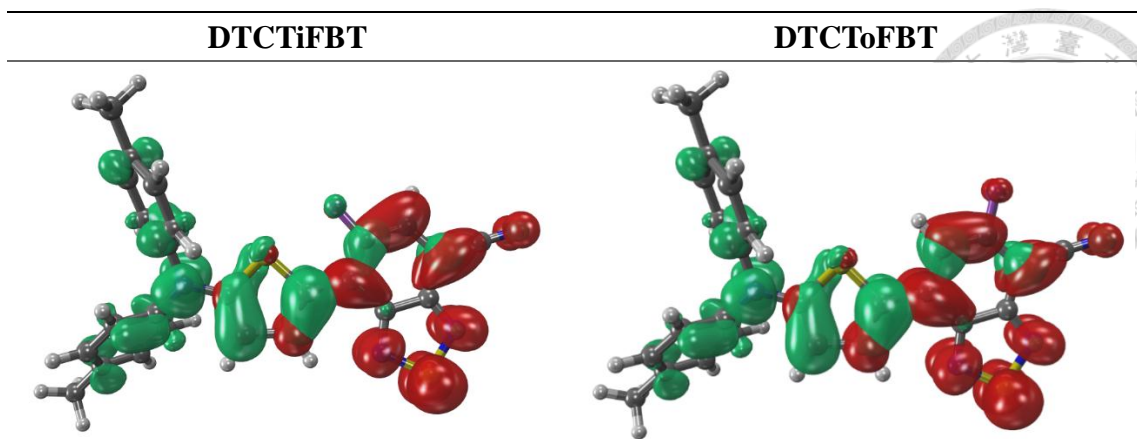


Figure 2-4. Isodensity surface plots of the HOMO (green) and LUMO (red) of **DTCTiFBT** and **DTCToFBT**.

2-5 Crystal Structures and Packings

The crystal of **DTCTiFBT** was obtained via biphasic diffusion between dichloromethane and methanol for X-ray analysis, and its crystal packing is illustrated in Figure 2-5. **DTCTiFBT** packs in parallel fashion in dimer with an average distance in the range of 3.34–3.45 Å, indicating benign intermolecular π - π interactions. However, the dimer lines in same direction with head to head orientation, thus creating net dipole moment. The uncanceled dipolarity could be involved in controlling charge transfer pathways, resulting in energetic disorder in OSCs.²⁷ In crystal packing, **DTCTiFBT** exhibits nearly perpendicular arrangement between neighboring molecules (the ditolylamine moiety was omitted for clarity.) Though no obvious conduction channel for charge carrier is found, the dipoles cancel in larger domain as illustrated. Moreover, a higher FF of 0.60 was reached for **DTCTiFBT**/C₆₀ OPV device, suggesting better morphologies in blending layer.

The dihedral angle between T and BT unit is 7.4° for **DTCTiFBT**, which is less than 7.7° for **DTCTB**.²⁶ Such observation is similar to the theoretical calculation in Section 2-4.

The crystals of **DTCToFBT** were obtained via biphasic diffusion between

chloroform or dichloromethane and methanol or pentane; however, they could not yield results under X-ray analysis, probably due to the soft and needle-like crystal nature.

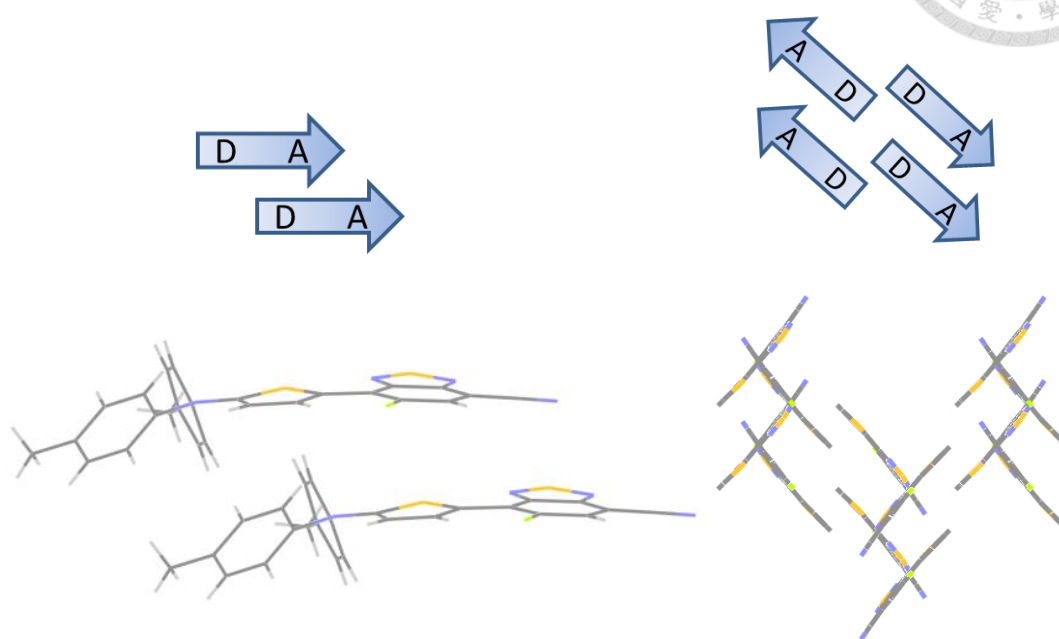


Figure 2-5. Crystal structures of **DTCTiFBT** in molecular packing.

2-6 Thermal Properties

Thermal stabilities and morphological properties of **DTCTiFBT** and **DTCToFBT** were investigated by thermogravimetric analysis (TGA) and differential scanning calorimetry (DSC), respectively. Their corresponding data are shown in Fig. SB1 – Fig. SB4. The decomposition temperatures (T_d) (referring to 5% weight loss) are 261–292 °C for these molecules. Thermal stability of materials is crucial for device fabrication under vacuum deposition. Although **DTCToFBT** shows lowest T_d and T_m among six molecules characterized in this thesis, it maintained the quality of vacuum deposited films and afforded efficient OPVs. To sum up, our D-A-A type molecular configuration could provide benign thermal stability for vacuum fabrication.

Table 2-4. Thermal parameters for **DTCTiFBT**, **DTCToFBT**, and **DTCTB**.

dyes	T _d (°C)	T _m (°C)
DTCTiFBT	290	211
DTCToFBT	261	192
DTCTB ²⁶	292	250

2-7 Photovoltaic and Electrochemical Impedance Characteristics

All molecules were subject to vacuum deposition with the OPV structure: ITO / MoO₃ (20 nm) / dye: C₆₀ (x nm) / C₆₀ (y nm) / bathocuproine (BCP) (7 nm) / Al (100 nm). MoO₃ and BCP were employed as a hole transporting layer and an electron transporting layer, respectively. The active layers comprised of D:A blend films and a thin neat electron acceptor film. The optimized device of **DTCTB** was repeated to eliminate factors of different time and cooperative partners from Dr. Hao-Chun Ting's result. The photovoltaic and electrochemical impedance characteristics were measured under simulated AM 1.5 G (100 mW cm⁻²) illumination. The ratio of dye: C₆₀ was varied from 1:1.6 to 1:2.6 via altering evaporation rate (Å/s) of dyes and C₆₀, and the total thickness of active layers (dye: C₆₀ / C₆₀) were varied from 60 nm to 90 nm, in search of best parameters for device performance. The optimized conditions and device performances are summarized in Table 2-5, and their current density-voltage (J-V) curves along with external quantum efficiency (EQE) spectra are shown in Figure 2-6. It is reasonable that the dye: C₆₀ ratio is 1:2.2 for all thiophene-based devices. Since we only did little change to each molecular backbone, the best mixing ratio along with the morphology in each D:A blend film are similar. Among all, **DTCToFBT**/C₆₀ OPV cell exhibited a V_{oc} of 0.83 V, a J_{sc} of 6.85 mA/cm², and a FF of 0.58, achieving a PCE of 3.28%, which outperformed counterpart **DTCTiFBT** and non-fluorinated **DTCTB**. Besides, **DTCTiFBT**/C₆₀ OPV cell exhibited a V_{oc} of 0.82 V, a J_{sc} of 6.33 mA/cm², and a higher FF of 0.60, achieving a PCE of 3.11%, which

still outperformed **DTCTB**. The lowered HOMO energy levels for **DTCTiFBT** and **DTCToFBT** account for the higher V_{oc} , and the bathochromic absorption resulted in the higher J_{sc} . As for EQE analyses, responses centered at 380–410 nm are contributed mainly by C_{60} were 55.8%, 52.6%, and 29.0% for **DTCTiFBT**, **DTCToFBT**, and **DTCTB**, respectively; responses centered at 585–598 nm mainly from dyes are 35.2%, 40.9%, and 30.9%, respectively. The former EQE response is stronger than the latter response for **DTCTiFBT** and **DTCToFBT**, due to the higher mixing ratio of C_{60} . We anticipate that raising the ratio of an electron donor will improve the 500–700 nm light utilizing efficiency. Further ratio and morphology control in D:A blend film are essential to enhance the performance of each electron donor in this chapter.

Table 2-5. Photovoltaic parameters for **DTCTiFBT**, **DTCToFBT**, and **DTCTB** with OPV structure: ITO / MoO₃ / dye: C₆₀ (x nm) / C₆₀ (y nm) / BCP / Al.

dyes	dye: C ₆₀	x, y (nm)	V_{oc} (V)	J_{sc} (mA/cm ²)	FF	PCE (%)	R_{sh} (k Ω cm ²)	R_s (Ω cm ²)
DTCTiFBT	1:2.2	70, 0	0.82	6.33	0.60	3.11	0.73	8.32
DTCToFBT	1:2.2	80, 0	0.83	6.85	0.58	3.28	0.75	11.74
DTCTB	1:2.2	60, 10	0.76	4.88	0.52	1.92	0.51	23.94

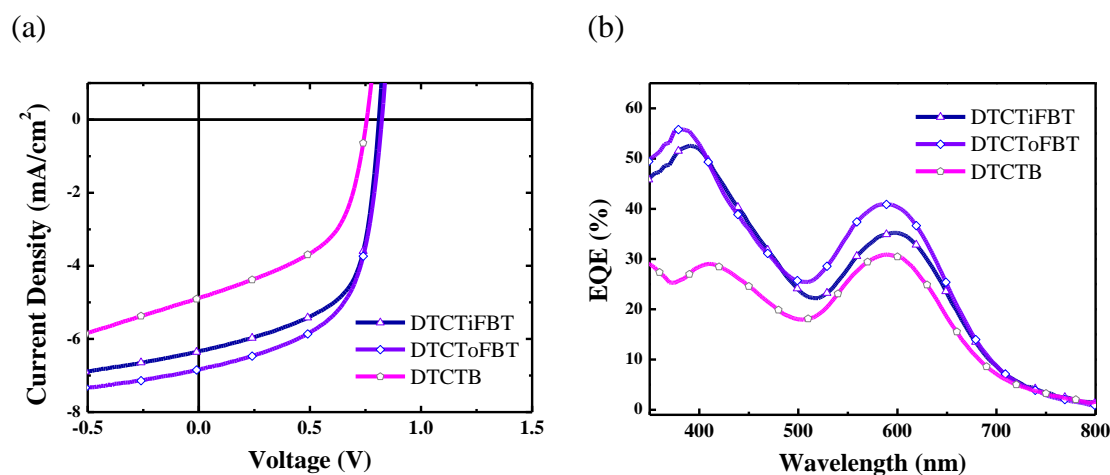


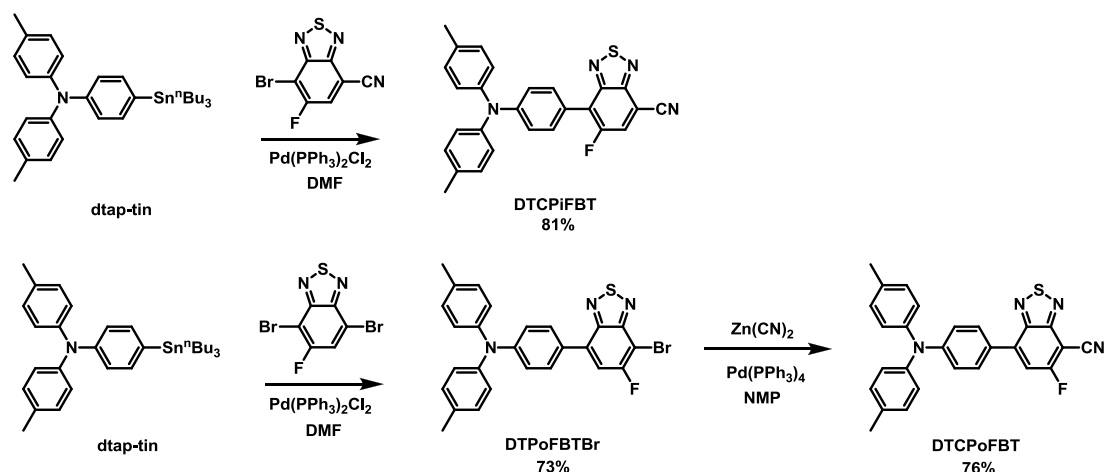
Figure 2-6. (a) J-V curves and (b) EQE spectra for **DTCTiFBT** (triangles), **DTCToFBT** (diamonds), and **DTCTB** (pentagons) for C₆₀-based OPV.



Chapter 3 DTCPiFBT and DTCPoFBT

3-1 Syntheses

The synthetic route of **DTCPiFBT** and **DTCPoFBT** is illustrated in Scheme 3-1. The procedure was similar to that of thiophene-based electron donors reported in Chapter 2, except that 4-(*N,N*-ditolylamino)-1-(tri-*n*-butylstannyl)phenylene (**dtap-tin**) was used as starting material. Stille coupling of **dtap-tin** and **FBTCN** directly afforded **DTCPiFBT** in 81% yield. Stille coupling of **dtap-tin** and **FBTBr** afforded **DTPoFBTBr** in 73% yield, which subsequently underwent Palladium-catalyzed cyanation to give **DTCPoFBT** in 76% yield.



Scheme 3-1. Synthetic route for **DTCPiFBT** and **DTCPoFBT**.

3-2 Optical Properties

Optical properties of **DTCPiFBT** and **DTCPoFBT** are shown in Figure 3-1. Photophysical and electrochemical properties of their and **DTCPB** are summarized in Table 3-1. In solution state, these molecules perform two bands absorption located at 300–350 nm and 400–600 nm. It is noteworthy that the extinction coefficient of the former band is larger than that of the latter band, which was also found for **DTCPB**.

Both **DTCPiFBT** and **DTCPoFBT** show slightly bathochromic shifts in absorption compared to **DTCPB** due to the introduction of a fluorine atom. In thin films, all molecules exhibit bathochromic shifts (19–23 nm) in their absorption maxima in the same trend as in solution state. However, all together, the phenylene-bridged electron donors exhibit 63–71 nm hypsochromic shifts as compared to thiophene-bridged counterparts because of the higher aromaticity of phenylene.⁶⁻⁷

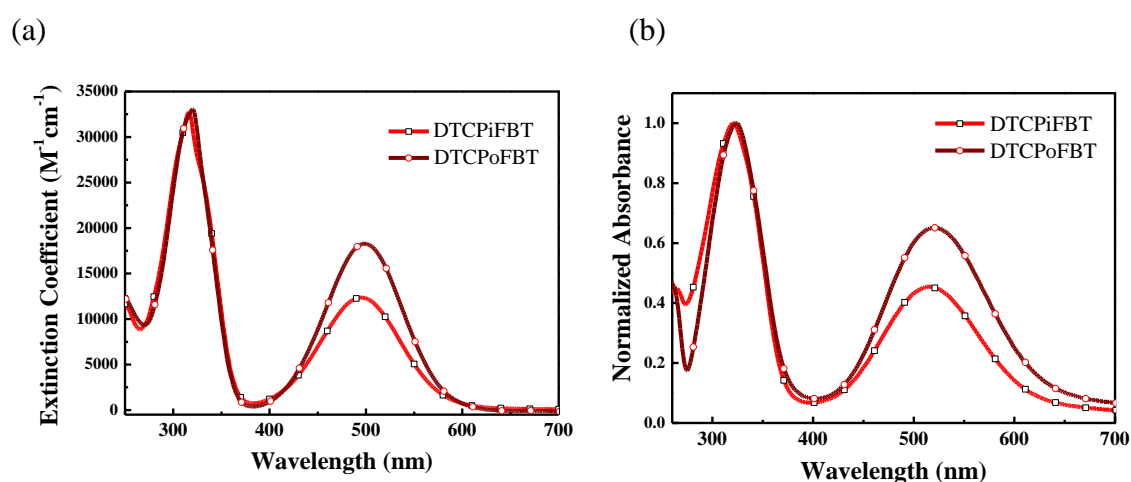


Figure 3-1. Absorption spectra of **DTCPiFBT** (square) and **DTCPoFBT** (circle) in (a) CH_2Cl_2 solutions and (b) vacuum deposited thin films.

Table 3-1. Photophysical and electrochemical parameters for **DTCPiFBT**, **DTCPoFBT**, and **DTCPB**.

dyes	λ_{max} soln (nm) (ϵ , $\text{M}^{-1} \text{cm}^{-1}$)	λ_{max} film (nm)	HOMO ^a (CV)(eV)	LUMO ^a (CV)(eV)	E_g^{CV} (eV)	IP ^b (eV)
DTCPiFBT	496 (12300)	515	-5.58	-3.59	1.99	5.56
	316 (32700)					
DTCPoFBT	498 (18300)	521	-5.67	-3.63	2.04	5.62
	320 (33200)					
DTCPB ²⁶	491 (18200)	511	-5.56	-3.52	2.04	5.51

^a HOMO (eV) = e [-5.1 - (E_{ox} - $E_{\text{Fc/Fc}^+}$)] & LUMO (eV) = e [-5.1 - (E_{red} - $E_{\text{Fc/Fc}^+}$)].^b

Determined by photoelectron spectrometer AC-2.

3-3 Electrochemical Properties

Cyclic voltammograms of **DTCPiFBT** and **DTCPoFBT** are shown in Figure 3-2. As shown in Table 3-1, both molecules perform lowered HOMO and LUMO as compared to **DTCPB** in both solution state and vacuum deposited thin films. Furthermore, **DTCPiFBT** shows narrowed bandgap, resulting from the much lowered LUMO energy level. **DTCPoFBT** exhibits same bandgap as **DTCPB**; however, the decrement of HOMO and LUMO energy levels are the highest among all newly synthesized electron donors in this thesis. The outward FBT linked to another cyano group could account for stronger electron withdrawing ability and thus stronger propensity for lowering HOMO and LUMO. Such propensity suggests that a higher V_{oc} can be achieved for **DTCPoFBT**.

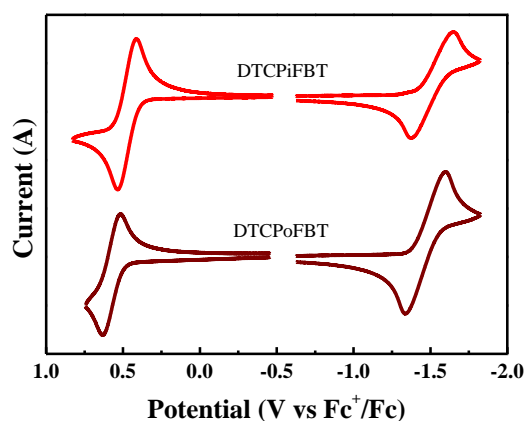


Figure 3-2. Cyclic voltammograms of **DTCPiFBT** and **DTCPoFBT**.

3-4 Theoretical Calculations

DFT and TD-DFT calculations were performed for **DTCPiFBT** and **DTCPoFBT** in CH_2Cl_2 . The optimized geometries for both molecules are showed in Table 3-3. Unlike thiophene-based electron donors mentioned in Chapter 2, all phenylene-based electron donors exhibit highly twisted conformation. The dihedral angles between phenylene (P) and benzothiadiazole (BT) units are 40.9° for

DTCPiFBT, 35.0° for **DTCPoFBT**, and 36.1° for **DTCPB**. The non-coplanarity is due to *ortho-ortho* steric interaction between P and BT units, which is greater for **DTCPiFBT** due to the larger size of an inward fluorine atom (1.35 \AA) than a hydrogen atom (1.20 \AA).

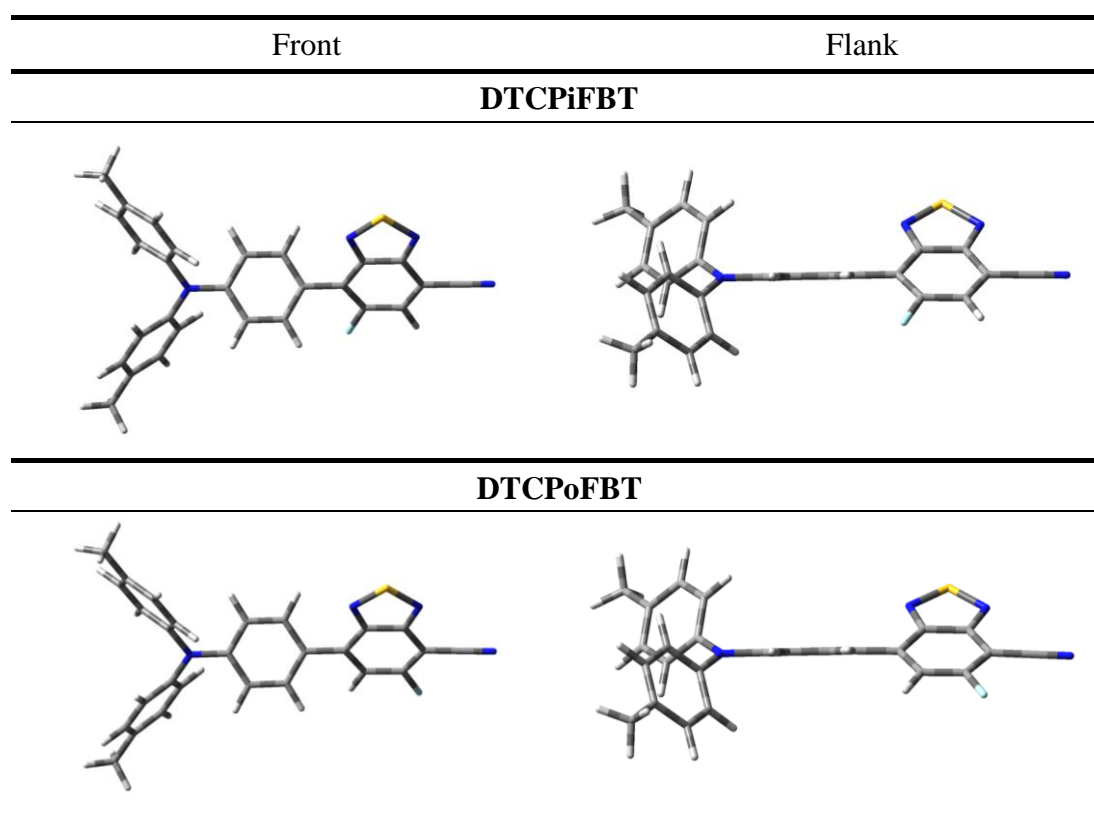


Figure 3-3. DFT-optimized geometries for **DTCPiFBT** and **DTCPoFBT**.

The dipole moments of **DTCPiFBT**, **DTCPoFBT**, and **DTCPB** are summarized in Table 3-2. The total dipole moments for all molecules are smaller as compared to the counterparts of thiophene-based molecules. Also, inward fluorination gives smaller dipole moment in both S_0 and S_1 , whereas outward fluorination gives larger dipole moment than non-fluorinated **DTCPB**. At the first excited state, because of charge separation caused by charge transfer, all molecules show larger dipole moment in same trend.

Table 3-2. Dipole moment parameters for **DTCPiFBT**, **DTCTPoFBT**, and **DTCPB**.

dyes	μ_g^a (D)	μ_e^b (D)	$\Delta\mu_{ge}^c$ (D)	μ_{tr}^d (D)
DTCPiFBT	8.05	10.62	2.58	8.04
DTCPoFBT	11.10	13.84	2.76	11.10
DTCPB	9.36	12.29	2.96	9.36

^a μ_g : total dipole moment at the ground state (S_0). ^b μ_e : total dipole moment at the first excited state (S_1). ^c $\Delta\mu_{ge}$: overall dipole moment change between S_0 and S_1 . ^d μ_{tr} : overall dipole moment overlap between S_0 and S_1 .

The absorption located at 400–600 nm corresponds mainly to transition from S_0 to S_1 , which is prominently constituted by the charge transfer excitation from HOMO to LUMO. However, the main absorption spanning 300–350 nm comprises several electronic transitions, which sums to larger oscillator strength. Such observation could be correlated to the twisted conformation phenylene-based molecules possess.

Table 3-3. TD-DFT calculated oscillator strengths, absorption wavelengths, molecular orbital compositions, and transition characters for **DTCPiFBT** and **DTCPoFBT**.

electronic transition	oscillator strength	$\lambda_{exp} / \lambda_{calc}$ (nm)	MO Composition	character
DTCPiFBT				
$S_0 \rightarrow S_1$	0.5657	496/430	9% HOMO - 1 \rightarrow LUMO 87% HOMO \rightarrow LUMO	$\pi - \pi^* + CT$ CT
$S_0 \rightarrow S_2$	0.0473		62% HOMO - 1 \rightarrow LUMO	$\pi - \pi^* + CT$
$S_0 \rightarrow S_3$	0.2106	316/284	56% HOMO \rightarrow LUMO + 2	CT
$S_0 \rightarrow S_4$	0.448		44% HOMO \rightarrow LUMO + 1	$\pi - \pi^* + CT$
DTCPoFBT				
$S_0 \rightarrow S_1$	0.6938	498/428	9% HOMO - 1 \rightarrow LUMO 87% HOMO \rightarrow LUMO	$\pi - \pi^* + CT$ CT
$S_0 \rightarrow S_2$	0.0099		64% HOMO - 1 \rightarrow LUMO	$\pi - \pi^* + CT$
$S_0 \rightarrow S_3$	0.0267	320/280	79% HOMO \rightarrow LUMO + 2	$\pi - \pi^*$
$S_0 \rightarrow S_4$	0.5630		64% HOMO \rightarrow LUMO + 1	$\pi - \pi^* + CT$

Though both molecules possess several electronic transitions, the most significant transition is from HOMO to LUMO via charge transfer. As shown in Figure 3-4, the benign separation between HOMO and LUMO is similar with thiophene-based molecules.

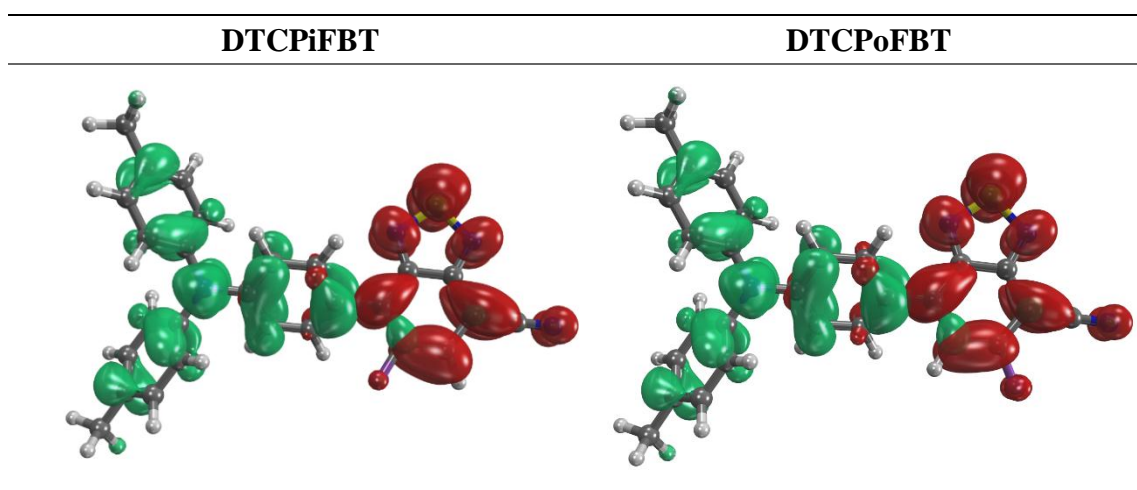


Figure 3-4. Isodensity surface plots of the HOMO (green) and LUMO (red) of **DTCPiFBT** and **DTCPoFBT**.

3-5 Crystal Structures and Packings

The crystals of **DTCPiFBT** and **DTCPoFBT** were easily obtained by slow evaporation of dichloromethane. Their crystal packings are illustrated in Figure 3-5. **DTCPiFBT** shows antiparallel fashion in dimer with an average distance in the range of 3.64–3.70 Å, indicating benign intermolecular π - π interactions (the residue solvent was omitted for clarity.) However, no obvious packing pattern in crystal grain was found. Unlike the antiparallel fashion for **DTCPiFBT** and **DTCPB**, the crystal of **DTCPoFBT** exhibits zig-zag orientation both in dimer and in crystal packing. Such observation is presumably correlated to vdW interaction between a fluorine atom and two hydrogen atoms on P unit, which was only found in **DTCPoFBT**. As a result, the distance between each dimer ranges 3.30–3.57 Å. Introduction of a fluorine atom can

provide more interaction in crystal packing concomitant with morphology alteration for the active layer in BHJ device.

The *ortho-ortho* steric interaction between P and BT induces the dihedral angles more than 27° (34.8° for **DTCPiFBT**, 29.7° for **DTCPoFBT**, and 27.3° for **DTCPB**²⁶). The larger dihedral angle of **DTCPiFBT** is due to the steric hindrance from the inward fluorine atom. The observation is similar to the results in Section 3-4.

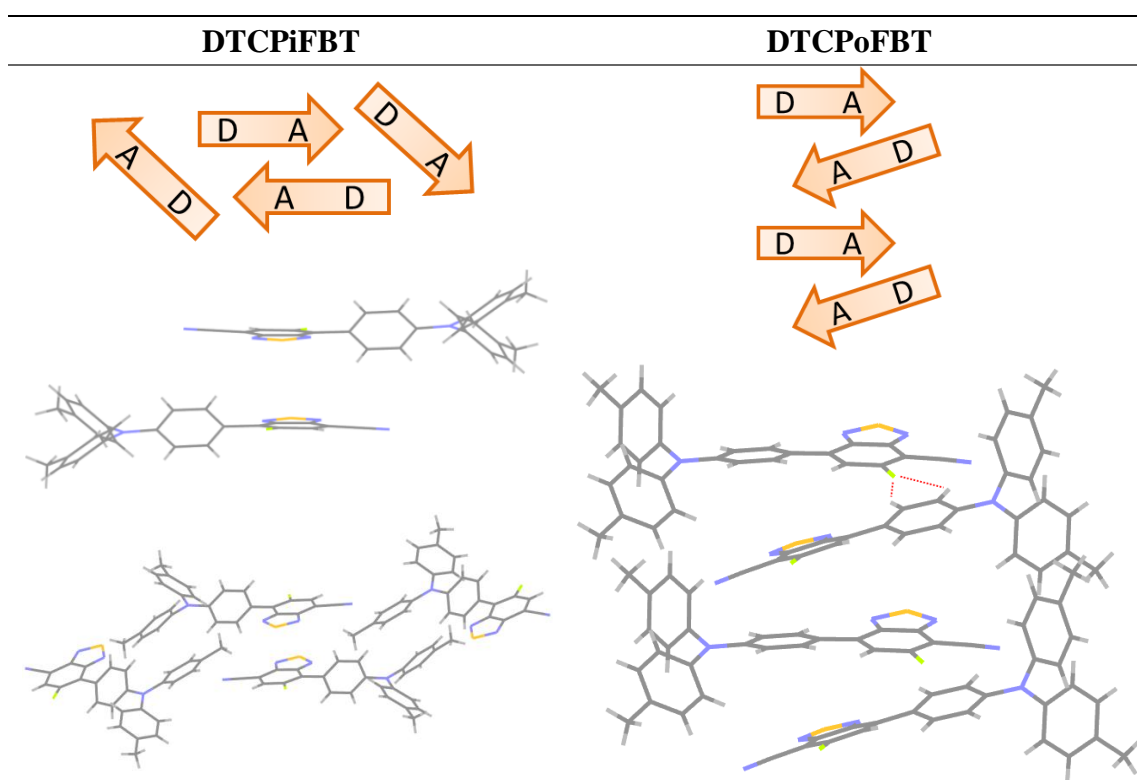


Figure 3-5. Crystal structures of **DTCPiFBT** and **DTCPoFBT** in molecular packing.

3-6 Thermal Properties

Thermal stabilities and morphological properties of **DTCPiFBT** and **DTCPoFBT** are shown in Fig. SB5 – Fig. SB8 and summarized in Table 3-4. The decomposition temperatures are above 270 °C for all molecules, which are suitable for vacuum fabrication. However, no distinct correlation for fluorination and the change in T_d and T_m was found.

Table 3-4. Thermal parameters for **DTCPiFBT**, **DTCPoFBT**, and **DTCPB**.

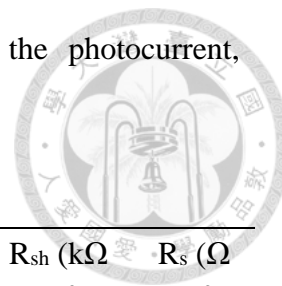
dyes	T _d (°C)	T _m (°C)
DTCPiFBT	272	209
DTCPoFBT	288	191
DTCPB ²⁶	287	204

3-7 Photovoltaic and Electrochemical Impedance Characteristics

DTCPiFBT and **DTCPoFBT** were subject to vacuum deposition with the OPV structure: ITO / MoO₃ (20 nm) / dye: C₆₀ (x nm) / BCP (7 nm) / Al (100 nm). The photovoltaic and electrochemical impedance characteristics were measured under simulated AM 1.5 G (100 mW cm⁻²) illumination. The device performances are summarized in Table 3-5, and their J-V curves along with EQE spectra are shown in Figure 3-6. **DTCPoFBT**/C₆₀ OPV cell exhibited a V_{oc} of 0.88 V, a J_{sc} of 6.50 mA/cm², and a high FF of 0.63, achieving a PCE of 3.62%. **DTCPiFBT**/C₆₀ OPV cell exhibited a V_{oc} of 0.89 V, a J_{sc} of 4.90 mA/cm², and a FF of 0.58, achieving a PCE of 2.65%. As for EQE analyses, responses centered at 380–400 nm contributed mainly by C₆₀ were 53.9% and 54.5% for **DTCPiFBT** and **DTCPoFBT**, respectively; responses centered at 530–535 nm mainly from dyes were 32.1%, and 42.7%, respectively. The former band is similar in intensity, whereas the latter band shows significant difference, as expected. Due to the highly twisted backbone of **DTCPiFBT**, its CT harvesting efficiency is lower than that of **DTCPoFBT**, resulting in inferior EQE response.

In summary, the tendency in V_{oc} of the new OPV devices in this thesis was coincident with the HOMO levels determined from cyclic voltammogram or AC-2. The low-lying HOMO level of **DTCPoFBT** resulted in a high V_{oc} of 0.88 V. However, the J_{sc} of **DTCPoFBT** was lower than that of **DTCToFBT** (6.85 mA/cm²) due to the larger bandgap of phenylene-based electron donors. The results demonstrated a trade-off between V_{oc} and J_{sc} for a series of D-A-A based devices. Among all,

DTCPoFBT stroke a balance between the photovoltage and the photocurrent, achieving a remarkable PCE of 3.62%.



dyes	dye: C ₆₀	x (nm)	V _{oc} (V)	J _{sc} (mA/cm ²)	FF	PCE (%)	R _{sh} (kΩ cm ²)	R _s (Ω cm ²)
DTCPiFBT	1:1.4	70	0.89	4.90	0.58	2.65	1.11	24.01
DTCPoFBT	1:1.8	70	0.88	6.50	0.63	3.62	1.28	17.19

Table 3-5. Photovoltaic parameters for **DTCPiFBT** and **DTCPoFBT** with OPV structure: ITO / MoO₃ / dye: C₆₀ (x nm) / BCP / Al.

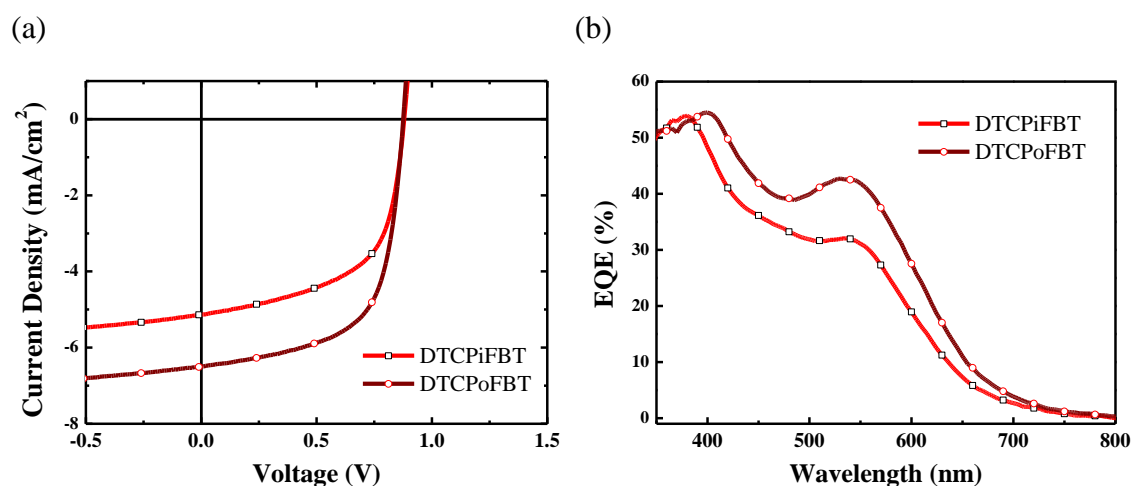


Figure 3-6. (a) J-V curves and (b) EQE spectra for **DTCPiFBT** (square), and **DTCPoFBT** (circle) for C₆₀-based OPV.

Encouraged by the promising results, we decide to replace the electron acceptor in pursuit of better device performance. C₇₀ is adopted to replace C₆₀ because of its broader optical absorption and higher extinction coefficient, which can provide better light-harvesting capabilities.²⁸ Besides, we expect a much higher V_{oc} can be reached for **DTCPoFBT** as optimizing conditions, which will improve morphology and reduce charge recombination. Further investigation of all newly synthesized electron donors in this thesis is in process.

Conclusions



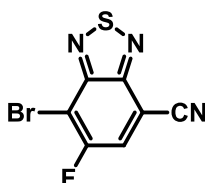
Our work characterized the effect of F-substituted benzothiadiazole unit on D-A-A structured small molecule electron donors. Though **DTCTiFBT** and **DTCToFBT** as well as **DTCPiFBT** and **DTCPoFBT** have regioisomeric nature, introduction of an inward or outward fluorine atom can alter dihedral angles and crystal packings by providing additional interactions or steric hindrance. All molecules show lowered HOMO and LUMO level and slightly red-shifted absorption as compared to those of the non-fluorinated counterparts, which are beneficial for pursuing higher V_{oc} and J_{sc} , respectively. Furthermore, all molecules possess benign thermal stability, high extinction coefficient, and appropriate energy levels suitable for OPV application. Among all, thiophene-bridged **DTCToFBT**/ C_{60} OPV cell exhibited a V_{oc} of 0.83 V, a J_{sc} of 6.85 mA/cm², and a FF of 0.58, achieving a PCE of 3.28%. Phenylene-bridged **DTCPoFBT**/ C_{60} OPV cell exhibited a V_{oc} of 0.88 V, a J_{sc} of 6.50 mA/cm², and a high FF of 0.63, achieving a remarkable PCE of 3.62%. All molecules are subject to further investigation.

Experiment Session



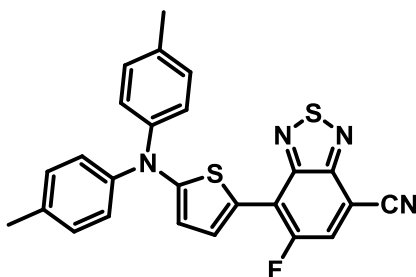
Syntheses and Materials.

All chemicals and reagents were used as received from commercial sources without purification. THF was dried by molecular sieves, and toluene was distilled by P₂O₅ as the drying agent. 4,7-dibromo-5-fluorobenzo[c][1,2,5]thiadiazole (**FBTBr**) was synthesized according to previous literature.¹⁵



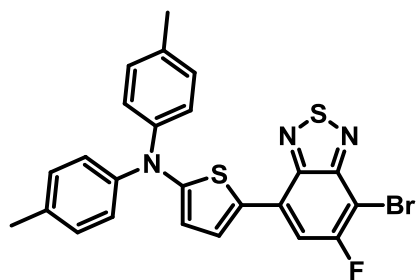
Synthesis of 4-bromo-7-cyano-5-fluorobenzo[c][1,2,5]thiadiazole (**FBTCN**)

A mixture of **FBTBr** (6.24 g, 20 mmol), Zn(CN)₂ (1.64 g, 14 mmol), and Pd(PPh₃)₄ (2.31 g, 2 mmol) in anhydrous *N*-methyl-2-pyrrolidone (NMP) (30 mL) was stirred and heated at 120 °C for 2 h under argon atmosphere. After cooled down to room temperature, the solution was poured to celite with ethyl acetate (EA) as eluent, followed by extraction with EA and brine several times to eliminate NMP. The crude product was purified by column chromatography with dichloromethane/hexane as eluent (v/v, 1:1) to afford **FBTCN** as a yellow solid (2.03 g, 39%), mp 143-144 °C; IR (KBr) 845, 876, 899, 1191, 1298, 1318, 1326, 1394, 1484, 1593, 1636, 2236, 3448 cm⁻¹; ¹H NMR (CDCl₃, 400 MHz) δ 7.94 (d, *J* = 8.0 Hz, 1H); ¹³C NMR (CDCl₃, 100 MHz) δ 159.2 (d, *J* = 254.5 Hz), 153.5 (d, *J* = 6.0 Hz), 149.4, 126.6 (d, *J* = 31.7 Hz), 113.6 (d, *J* = 2.7 Hz), 105.9 (d, *J* = 24.1 Hz), 105.1 (d, *J* = 10.1 Hz); ¹⁹F NMR (CDCl₃, 376 MHz) δ -102.2 (d, *J* = 7.9 Hz, 1F); HRMS (*m/z*, FAB⁺) Calcd for C₇H⁷⁹BrFN₃S 256.9059 found 256.9055, Calcd for C₇H⁸¹BrFN₃S 258.9038 found 258.9037.



Synthesis of **DTCTiFBT**

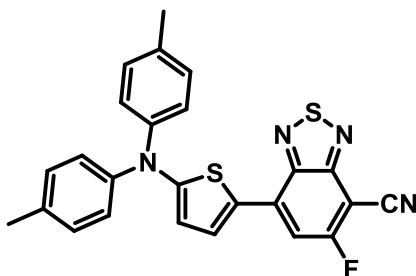
A mixture of 4-(*N,N*-ditolylamino)-1-(tri-*n*-butylstannyl)thiophene (7 mmol), **FBTCN** (1716 mg, 6.65 mmol), and PdCl₂(PPh₃)₂ (246 mg, 0.35 mmol) in anhydrous toluene (22 mL) was stirred and heated at 120 °C for 3 h under argon atmosphere. After cooled down to room temperature, the solvent was removed by rotary evaporation. The crude product was further purified by column chromatography with dichloromethane/hexane as eluent (v/v, 1:2). **DTCTiFBT** was obtained as a purple solid (2342 mg, 77%), mp 211 °C (DSC); IR (KBr) 1156, 1328, 1360, 1389, 1434, 1507, 2222, 2860, 2921, 3040 cm⁻¹; ¹H NMR (CDCl₃, 400 MHz) δ 8.25 (d, *J* = 4 Hz, 1H), 7.85 (d, *J* = 12 Hz, 1H), 7.14-7.20 (m, 8H), 6.54 (dd, *J* = 4.5, 1.5 Hz, 1H), 2.36 (s, 6H); ¹³C NMR (CDCl₃, 100 MHz) δ 160.5 (d, *J* = 9.1 Hz), 155.3 (d, *J* = 252.4 Hz), 151.9 (d, *J* = 11.1 Hz), 151.0, 144.4, 134.9, 134.0 (d, *J* = 10.1 Hz), 130.2, 126.9 (d, *J* = 33.2 Hz), 124.8, 119.7 (d, *J* = 7.0 Hz), 119.3 (d, *J* = 14.1 Hz), 115.0, 114.2, 98.5 (d, *J* = 12.1 Hz), 21.0; ¹⁹F NMR (CDCl₃, 376 MHz) δ -112.0 (d, *J* = 12.4 Hz, 1F) HRMS (*m/z*, FAB⁺) Calcd for C₂₅H₁₇FN₄S₂ 456.0879 found 456.0883.



Synthesis of **DTToFBTBr**

A mixture of 4-(*N,N*-ditolylamino)-1-(tri-*n*-butylstannyl)thiophene (1.5 mmol),

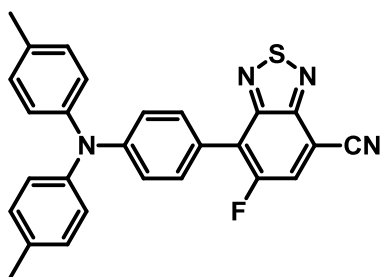
FBTBr (468 mg, 1.5 mmol), and $\text{PdCl}_2(\text{PPh}_3)_2$ (53 mg, 0.075 mmol) in anhydrous toluene (4.7 mL) was stirred and refluxed overnight under argon atmosphere. After cooled down to room temperature, the solvent was removed by rotary evaporation. The crude product was further purified by column chromatography with dichloromethane/hexane as eluent (v/v, 1:4). **DTToFBTBr** was obtained as a black solid (510 mg, 67%), mp 178-180 °C; IR (KBr) 813, 1291, 1454, 1511, 1593, 1667, 2864, 2913, 3023 cm^{-1} ; ^1H NMR (CDCl_3 , 400 MHz) δ 7.98 (d, $J = 4$ Hz, 1H), 7.42 (d, $J = 12$ Hz, 1H), 7.11-7.16 (m, 8H), 6.54 (d, $J = 4$ Hz, 1H), 2.35 (s, 6H); ^{13}C NMR (CDCl_3 , 100 MHz) δ 160.9 (d, $J = 251.4$ Hz), 156.7, 154.3, 149.0, 144.8, 134.2, 130.1, 129.5, 128.0 (d, $J = 11.1$ Hz), 126.7, 124.1, 116.2, 113.7 (d, $J = 30.2$ Hz), 93.8, 20.9; ^{19}F NMR (CDCl_3 , 376 MHz) δ -104.3 (d, $J = 11.3$ Hz, 1F); HRMS (m/z , FAB^+) Calcd for $\text{C}_{26}\text{H}_{19}^{79}\text{BrFN}_3\text{S}$ 509.0031 found 509.0034, Calcd for $\text{C}_{26}\text{H}_{19}^{81}\text{BrFN}_3\text{S}$ 511.0011 found 511.0010.



Synthesis of **DTCToFBT**

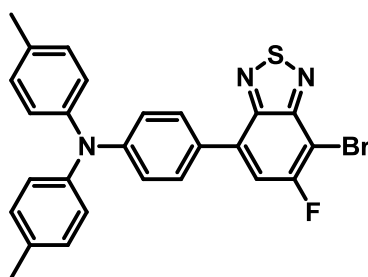
A mixture of **DTToFBTBr** (306 mg, 0.6 mmol), $\text{Zn}(\text{CN})_2$ (49 mg, 0.42 mmol), $\text{Pd}(\text{PPh}_3)_4$ (55 mg, 0.048 mmol) in degassed NMP (6 mL) was stirred and heated at 120 °C for 2 h under argon atmosphere. After cooled down to room temperature, the solution was extracted with EA and brine several times to remove NMP. The crude product was purified by column chromatography with dichloromethane/hexane as eluent (v/v, 1:1) to afford **DTCToFBT** as a purple solid (240 mg, 89%), mp 192 °C (DSC); IR (KBr) 1054, 1156, 1217, 1348, 1442, 1507, 1552, 2227, 2860, 2921, 3032

cm⁻¹; ¹H NMR (CDCl₃, 400 MHz) δ 8.17 (d, *J* = 4 Hz, 1H), 7.29 (d, *J* = 12 Hz, 1H), 7.16-7.21 (m, 8H), 6.48 (d, *J* = 4 Hz, 1H), 2.37 (s, 6H); ¹³C NMR (CDCl₃, 100 MHz) δ 167.0 (d, *J* = 264.5 Hz), 160.7, 153.9 (d, *J* = 8.0 Hz), 148.6, 144.0, 135.5, 133.9 (d, *J* = 12.1 Hz), 133.2, 130.3, 125.0, 124.1, 114.0, 111.8, 110.3 (d, *J* = 27.2 Hz), 86.1 (d, *J* = 19.1 Hz), 21.0; ¹⁹F NMR (CDCl₃, 376 MHz) δ -99.8 (d, *J* = 10.5 Hz, 1F); HRMS (*m/z*, FAB⁺) Calcd for C₂₅H₁₇FN₄S₂ 456.0879 found 456.0886.



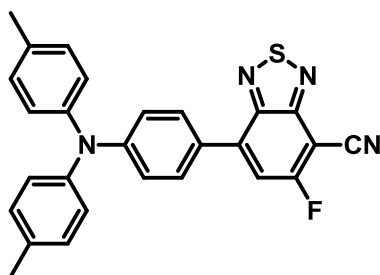
Synthesis of **DTCPiFBT**

A mixture of 4-(*N,N*-ditolylamino)-1-(tri-*n*-butylstannyl)phenylene (9 mmol), **FBTCN** (2207 mg, 8.55 mmol), and PdCl₂(PPh₃)₂ (316 mg, 0.45 mmol) in anhydrous toluene (28 mL) was stirred and heated at 120 °C for 3 h under argon atmosphere. After cooled down to room temperature, the solvent was removed by rotary evaporation. The crude product was further purified by column chromatography with dichloromethane/hexane as eluent (v/v, 1:2). **DTCPiFBT** was obtained as a black solid (3131 mg, 81%), mp 209 °C (DSC); IR (KBr) 817, 1156, 1332, 1487, 1507, 1548, 1601, 2235, 2860, 2921, 3023, 3056 cm⁻¹; ¹H NMR (CDCl₃, 400 MHz) δ 7.96 (d, *J* = 10.1 Hz, 1H), 7.69 (dd, *J* = 8.8, 1.6 Hz, 2H), 7.09-7.14 (m, 10H), 2.34 (s, 6H), ¹³C NMR (CDCl₃, 100 MHz) δ 157.1 (d, *J* = 251.4 Hz), 153.9 (d, *J* = 10.1 Hz), 150.8, 149.7, 144.3, 134.0, 131.5 (d, *J* = 4.0 Hz), 130.2, 127.6 (d, *J* = 33.2 Hz), 125.8, 124.8 (d, *J* = 15.1 Hz), 121.0, 119.7, 114.5, 102.7 (d, *J* = 12.1 Hz), 20.9; ¹⁹F NMR (CDCl₃, 376 MHz) δ -115.0 (d, *J* = 10.5 Hz, 1F); HRMS (*m/z*, FAB⁺) Calcd for C₂₇H₁₉FN₄S 450.1314 found 450.1306.



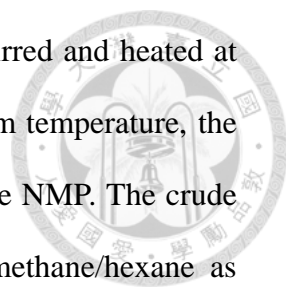
Synthesis of **DTPoFBTBr**

A mixture of 4-(*N,N*-ditolylamino)-1-(tri-*n*-butylstannyl)phenylene (1.5 mmol), **FBTBr** (468 mg, 1.5 mmol), and PdCl₂(PPh₃)₂ (53 mg, 0.075 mmol) in anhydrous toluene (4.7 mL) was stirred and refluxed overnight under argon atmosphere. After cooled down to room temperature, the solvent was removed by rotary evaporation. The crude product was further purified by column chromatography with dichloromethane/hexane as eluent (v/v, 1:4). **DTPoFBTBr** was obtained as an orange solid (550 mg, 73%), mp 153-156 °C; IR (KBr) 816, 1208, 1273, 1295, 1481, 1506, 1597, 2919, 3026 cm⁻¹; ¹H NMR (CDCl₃, 400 MHz) δ 7.77-7.80 (m, 2H), 7.53 (d, *J* = 8.0 Hz, 1H), 7.07-7.13 (m, 10H), 2.35 (s, 6H); ¹³C NMR (CDCl₃, 100 MHz) δ 161.0 (d, *J* = 252.4 Hz), 154.4 (d, *J* = 7.4 Hz), 150.3, 149.4, 144.5, 134.3 (d, *J* = 10.2 Hz), 133.6, 130.1, 129.9, 127.3, 125.5, 120.9, 117.6 (d, *J* = 30.3 Hz), 95.6 (d, *J* = 24.2 Hz), 20.9; ¹⁹F NMR (CDCl₃, 376 MHz) δ -104.1 (d, *J* = 7.5 Hz, 1F); HRMS (*m/z*, FAB⁺) Calcd for C₂₆H₁₉⁷⁹BrFN₃S 503.0467 found 503.0457, Calcd for C₂₆H₁₉⁸¹BrFN₃S 505.0447 found 505.0448.



Synthesis of **DTCPoFBT**

A mixture of **DTPoFBTBr** (2600 mg, 5.15 mmol), Zn(CN)₂ (424 mg, 3.61 mmol),



Pd(PPh₃)₄ (477 mg, 0.41 mmol) in degassed NMP (52 mL) was stirred and heated at 120 °C for 2 h under argon atmosphere. After cooled down to room temperature, the solution was extracted with EA and brine several times to eliminate NMP. The crude product was purified by column chromatography with dichloromethane/hexane as eluent (v/v, 1:1) to afford **DTCPoFBT** as a red solid (1758 mg, 76%), mp 191 °C (DSC); IR (KBr) 813, 1221, 1336, 1483, 1520, 1556, 1601, 2231, 2864, 2917, 3040 cm⁻¹; ¹H NMR (CDCl₃, 400 MHz) δ 7.86-7.88 (m, 2H), 7.54 (d, *J* = 8.0 Hz, 1H), 7.08-7.15 (m, 10H), 2.35 (s, 6H); ¹³C NMR (CDCl₃, 100 MHz) δ 166.9 (d, *J* = 265.5 Hz), 153.9 (d, *J* = 8.0 Hz), 150.6, 150.1, 144.0, 140.6 (d, *J* = 11.1 Hz), 134.3, 130.4, 130.2, 126.0, 125.9, 120.0, 115.6 (d, *J* = 27.2 Hz), 111.3, 88.8 (d, *J* = 18.1 Hz), 20.9; ¹⁹F NMR (CDCl₃, 376 MHz) δ -98.9 (d, *J* = 12.0 Hz, 1F); HRMS (*m/z*, FAB⁺) Calcd for C₂₇H₁₉FN₄S 450.1314 found 450.1316.

General Experiment



Nuclear Magnetic Resonance Spectroscopy, NMR

^1H , ^{13}C , and ^{19}F NMR were measured by Varian 400 unity plus (400 MHz), using CDCl_3 as solvent. The Chemical shift δ was reported in ppm. The definition of splitting pattern was: s, singlet; d, doublet; t, triplet; q, quartet; qn, quintet; sex, sextet; m, multiplet. Coupling constant was represented by J and reported in Hz.

Infrared Spectroscopy, IR

The IR spectra were measured by OMNIC 8.0 spectrometer, and the recorded wavenumbers were reported in cm^{-1} . Samples were dissolved in CH_2Cl_2 and dropped onto KBr and dried prior to use.

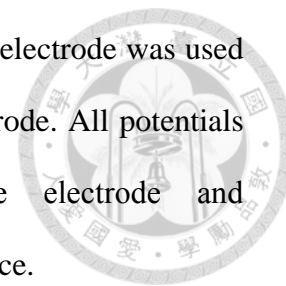
Ultraviolet–Visible Spectroscopy, UV

The absorption spectra in CH_2Cl_2 were measured by JASCO V-670 spectrophotometer. Three different concentrations ranging from 10^{-6} to 10^{-7} M in CH_2Cl_2 were measured in order to obtain the UV-Vis spectrum and the extinction coefficient. The absorption spectra of thin films were measured by Hitachi U4100.

Cyclic Voltammetry, CV

Cyclic voltammetry spectra were recorded in 0.1 M of substrate on a CHI619B electrochemical analyzer. Oxidation CV measurements were carried out in anhydrous CH_2Cl_2 containing 0.1 M tetrabutylammonium hexafluorophosphate (TBAPF_6) as a supporting electrolyte. Reduction CV measurements were conducted in anhydrous THF with 0.1 M tetrabutylammonium perchlorate (TBAP) as a supporting electrolyte

and purging with argon for 5 minutes prior to experiment. Carbon electrode was used as the working electrode and a platinum wire as the counter electrode. All potentials were recorded versus Ag/AgCl (sat'd) as a reference electrode and ferrocenium/ferrocene redox couple was used as an internal reference.



Theoretical Calculations

The electronic and optical properties and optimized conformation were estimated by density function theory (DFT) and time-dependent density function theory (TD-DFT) calculations in CH₂Cl₂ using CAM-B3LYP function with the 6-311G(d,p) basis set.

Mass Spectroscopy, MS

The high resolution mass spectra were measured by spectrometer JEOL SX-102A using fast atom bombardment as the ionization method.

Differential scanning calorimetry, DSC

Differential scanning calorimetry analyses were performed on a TA Instrument 2920 MDSC V2.6A Low-Temperature Difference Scanning Calorimeter. The spectra were recorded at a heating rate of 10 °C/min with nitrogen flushing.

Thermogravimetric analyses, TGA

Thermogravimetric analyses were performed on a TA Instrument Dynamic Q500 at a heating rate of 10 °C/min with nitrogen flushing.

Photocurrent-Voltage Measurement

The photocurrent-voltage characteristics of the photovoltaics were measured under illumination of AM1.5G solar light (100 mW/cm²) from a solar simulator (Newport

model 91195A). An electrical source meter (Keithley 2400) was employed to record the photocurrents of the device under different voltage.



External Quantum Efficiency Measurement, EQE

The external quantum efficiency measurement system consisted of a source meter (Keithley 2400), a solar simulator, a wavelength selectable arc lamp (A-1010B Arc Lamp Housing), and a monochromator (Newport model 74100). The signals were amplified by a lock-in amplifier (Signal Recovery model 7265). The photocurrents from the OPV device were measured through the lock-in amplifier, and the number of electrons and holes generated in different wavelength can be calculated.



References

1. Nayak, P. K.; Cahen, D., *Adv. Mater.* **2014**, *26*, 1622.
2. (a) Gao, F.; Wang, Y.; Shi, D.; Zhang, J.; Wang, M.; Jing, X.; Humphry-Baker, R.; Wang, P.; Zakeeruddin, S. M.; Grätzel, M., *J. Am. Chem. Soc.* **2008**, *130*, 10720; (b) Yu, Q.; Wang, Y.; Yi, Z.; Zu, N.; Zhang, J.; Zhang, M.; Wang, P., *ACS Nano* **2010**, *4*, 6032; (c) Yella, A.; Lee, H.-W.; Tsao, H. N.; Yi, C.; Chandiran, A. K.; Nazeeruddin, M. K.; Diau, E. W.-G.; Yeh, C.-Y.; Zakeeruddin, S. M.; Grätzel, M., *Science* **2011**, *334*, 629.
3. Dou, L.; You, J.; Hong, Z.; Xu, Z.; Li, G.; Street, R. A.; Yang, Y., *Adv. Mater.* **2013**, *25*, 6642.
4. Roncali, J., *Acc. Chem. Res.* **2009**, *42*, 1719.
5. Architectural Record's Continuing Education Center.
<http://continuingeducation.construction.com/article.php?L=68&C=488&P=6>.
6. Cheng, Y.-J.; Yang, S.-H.; Hsu, C.-S., *Chem. Rev.* **2009**, *109*, 5868.
7. Aromaticity.
<http://www.mhhe.com/physsci/chemistry/carey/student/olc/graphics/carey04oc/ref/ch11aromaticity.html>.
8. Lin, L.-Y.; Chen, Y.-H.; Huang, Z.-Y.; Lin, H.-W.; Chou, S.-H.; Lin, F.; Chen, C.-W.; Liu, Y.-H.; Wong, K.-T., *J. Am. Chem. Soc.* **2011**, *133*, 15822.
9. Ma, W.; Yang, C.; Gong, X.; Lee, K.; Heeger, A. J., *Adv. Funct. Mater.* **2005**, *15*, 1617.
10. (a) Brabec, C. J.; Cravino, A.; Meissner, D.; Sariciftci, N. S.; Fromherz, T.; Rispen, M. T.; Sanchez, L.; Hummelen, J. C., *Adv. Funct. Mater.* **2001**, *11*, 374; (b) Scharber, M. C.; Mühlbacher, D.; Koppe, M.; Denk, P.; Waldauf, C.; Heeger, A. J.;

Brabec, C. J., *Adv. Mater.* **2006**, *18*, 789.

11. Kan, B.; Zhang, Q.; Li, M.; Wan, X.; Ni, W.; Long, G.; Wang, Y.; Yang, X.; Feng, H.; Chen, Y., *J. Am. Chem. Soc.* **2014**, *136*, 15529.

12. (a) Zou, Y.; Holst, J.; Zhang, Y.; Holmes, R. J., *J. Mater. Chem. A* **2014**, *2*, 12397;

(b) Chen, Y. H.; Lin, L. Y.; Lu, C. W.; Lin, F.; Huang, Z. Y.; Lin, H. W.; Wang, P. H.; Liu, Y. H.; Wong, K. T.; Wen, J.; Miller, D. J.; Darling, S. B., *J. Am. Chem. Soc.* **2012**, *134*, 13616.

13. Cnops, K.; Rand, B. P.; Cheyns, D.; Verreert, B.; Empl, M. A.; Heremans, P., *Nat. Commun.* **2014**, *5*, 3406.

14. Shim, H.-S.; Lin, F.; Kim, J.; Sim, B.; Kim, T.-M.; Moon, C.-K.; Wang, C.-K.; Seo, Y.; Wong, K.-T.; Kim, J.-J., *Adv. Energy Mater.* **2015**, *5*, DOI: 10.1002/aenm.201500228.

15. van der Poll, T. S.; Love, J. A.; Nguyen, T. Q.; Bazan, G. C., *Adv. Mater.* **2012**, *24*, 3646.

16. Gupta, V.; Kyaw, A. K.; Wang, D. H.; Chand, S.; Bazan, G. C.; Heeger, A. J., *Sci. Rep.* **2013**, *3*, 1965.

17. Takacs, C. J.; Sun, Y.; Welch, G. C.; Perez, L. A.; Liu, X.; Wen, W.; Bazan, G. C.; Heeger, A. J., *J. Am. Chem. Soc.* **2012**, *134*, 16597.

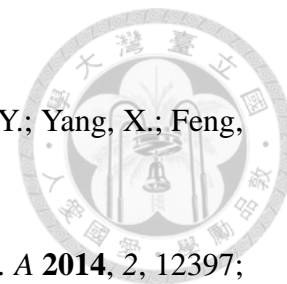
18. Wang, J.-L.; Yin, Q.-R.; Miao, J.-S.; Wu, Z.; Chang, Z.-F.; Cao, Y.; Zhang, R.-B.; Wang, J.-Y.; Wu, H.-B.; Cao, Y., *Adv. Funct. Mater.* **2015**, *25*, 3514.

19. He, Z.; Zhong, C.; Su, S.; Xu, M.; Wu, H.; Cao, Y., *Nature Photon.* **2012**, *6*, 593.

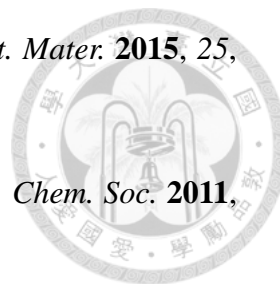
20. Jung, J. W.; Jo, J. W.; Chueh, C. C.; Liu, F.; Jo, W. H.; Russell, T. P.; Jen, A. K., *Adv. Mater.* **2015**, *27*, 3310.

21. Liu, X.; Sun, Y.; Hsu, B. B.; Lorbach, A.; Qi, L.; Heeger, A. J.; Bazan, G. C., *J. Am. Chem. Soc.* **2014**, *136*, 5697.

22. Zhang, M.; Guo, X.; Zhang, S.; Hou, J., *Adv. Mater.* **2014**, *26*, 1118.



23. Jo, J. W.; Bae, S.; Liu, F.; Russell, T. P.; Jo, W. H., *Adv. Funct. Mater.* **2015**, *25*, 120.
24. Price, S. C.; Stuart, A. C.; Yang, L.; Zhou, H.; You, W., *J. Am. Chem. Soc.* **2011**, *133*, 4625.
25. Characteristic IR Absorption Frequencies of Organic Functional Groups.
<http://www2.ups.edu/faculty/hanson/Spectroscopy/IR/IRfrequencies.html>.
26. Ting, H.-C. Design, Synthesis, and Characterization of Small-Molecule Materials for Organic Solar Cells. National Taiwan University, 2014.
27. Burckstummer, H.; Tulyakova, E. V.; Deppisch, M.; Lenze, M. R.; Kronenberg, N. M.; Gsanger, M.; Stolte, M.; Meerholz, K.; Wurthner, F., *Angew. Chem., Int.* **2011**, *50*, 11628.
28. Chiu, S.-W.; Lin, L.-Y.; Lin, H.-W.; Chen, Y.-H.; Huang, Z.-Y.; Lin, Y.-T.; Lin, F.; Liu, Y.-H.; Wong, K.-T., *Chem. Commun.* **2012**, *48*, 1857.





Appendix A

^1H and ^{13}C NMR Spectra

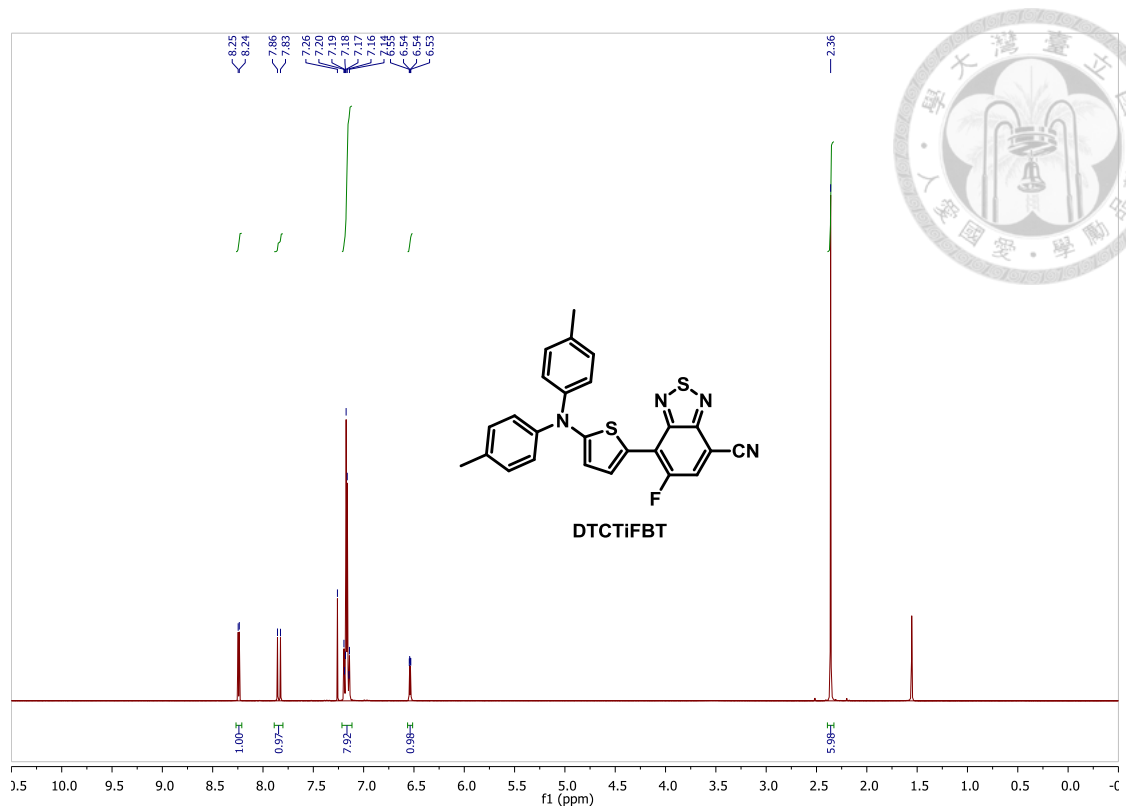


Fig. SA1. ^1H NMR spectrum of DTCTiFBT.

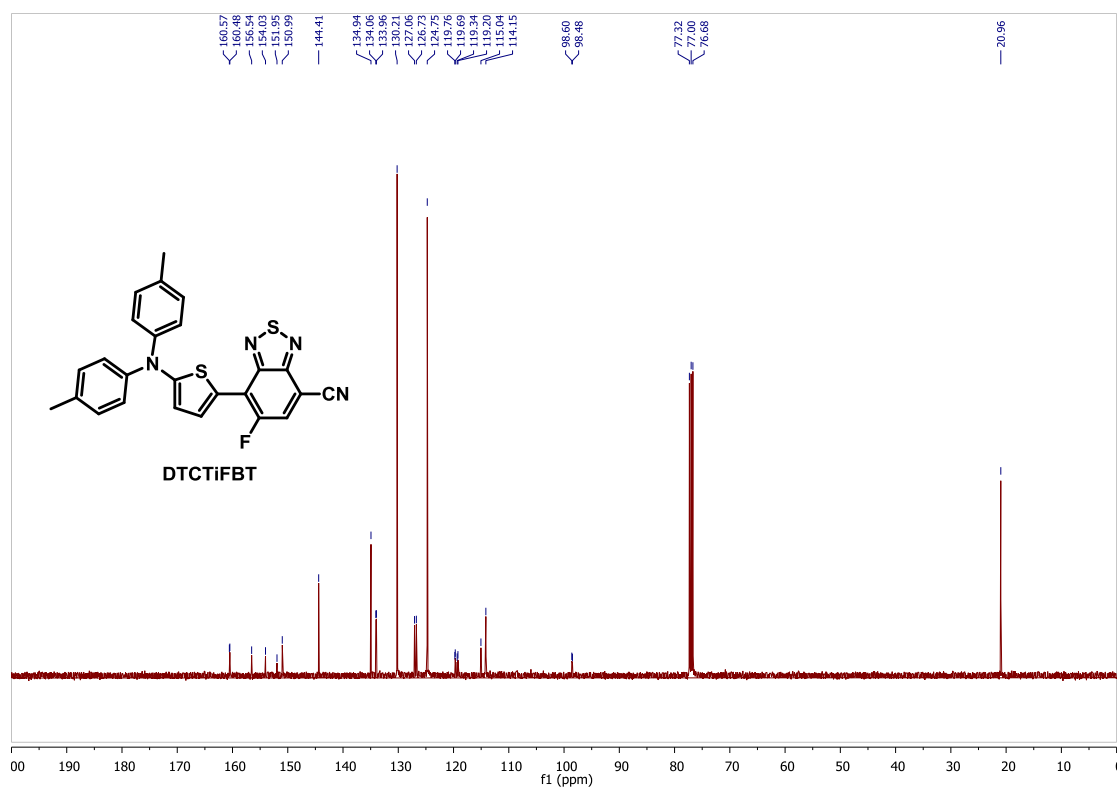


Fig. SA2. ^{13}C NMR spectrum of DTCTiFBT.

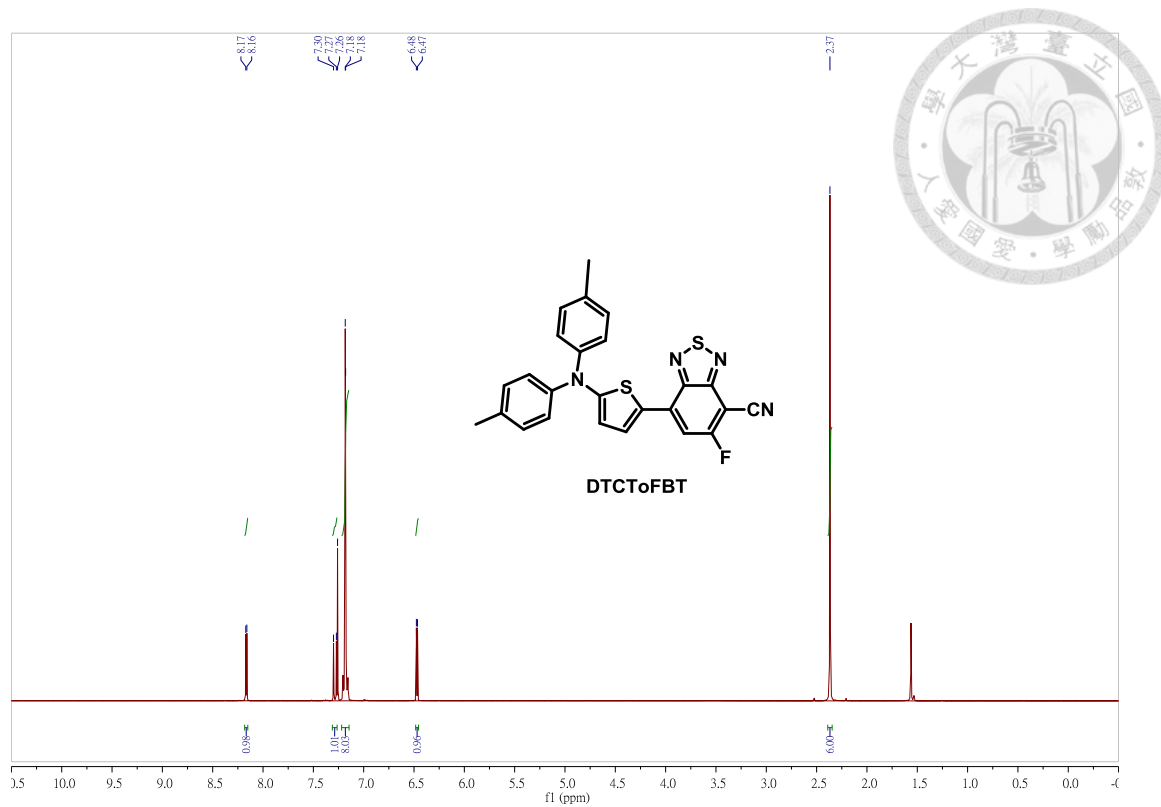


Fig. SA3. ¹H NMR spectrum of DTCToFBT.

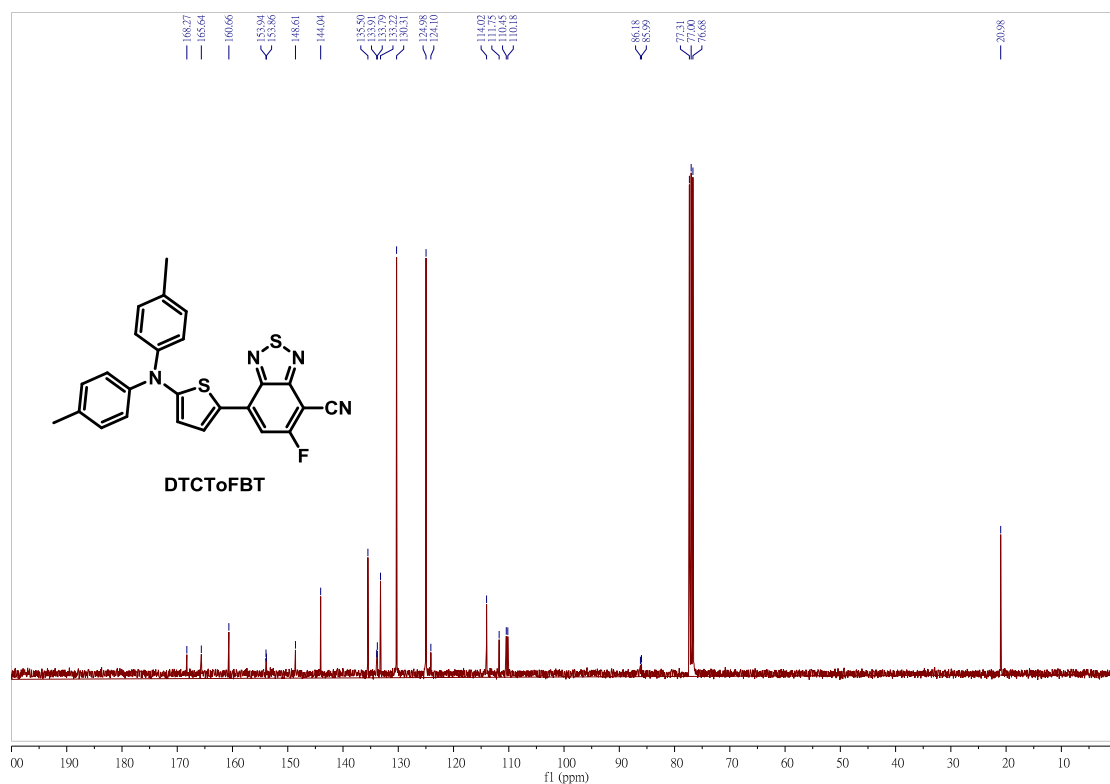


Fig. SA4. ¹³C NMR spectrum of DTCToFBT.

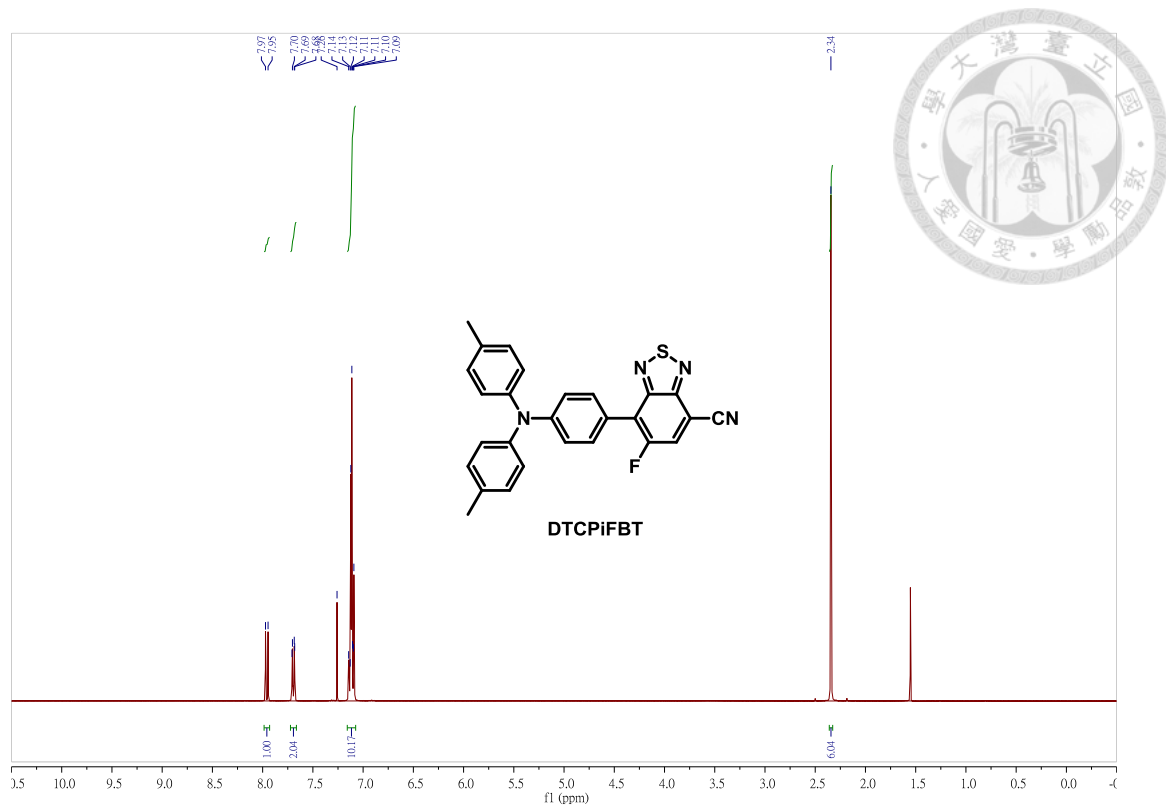


Fig. SA5. ¹H NMR spectrum of DTCPiFBT.

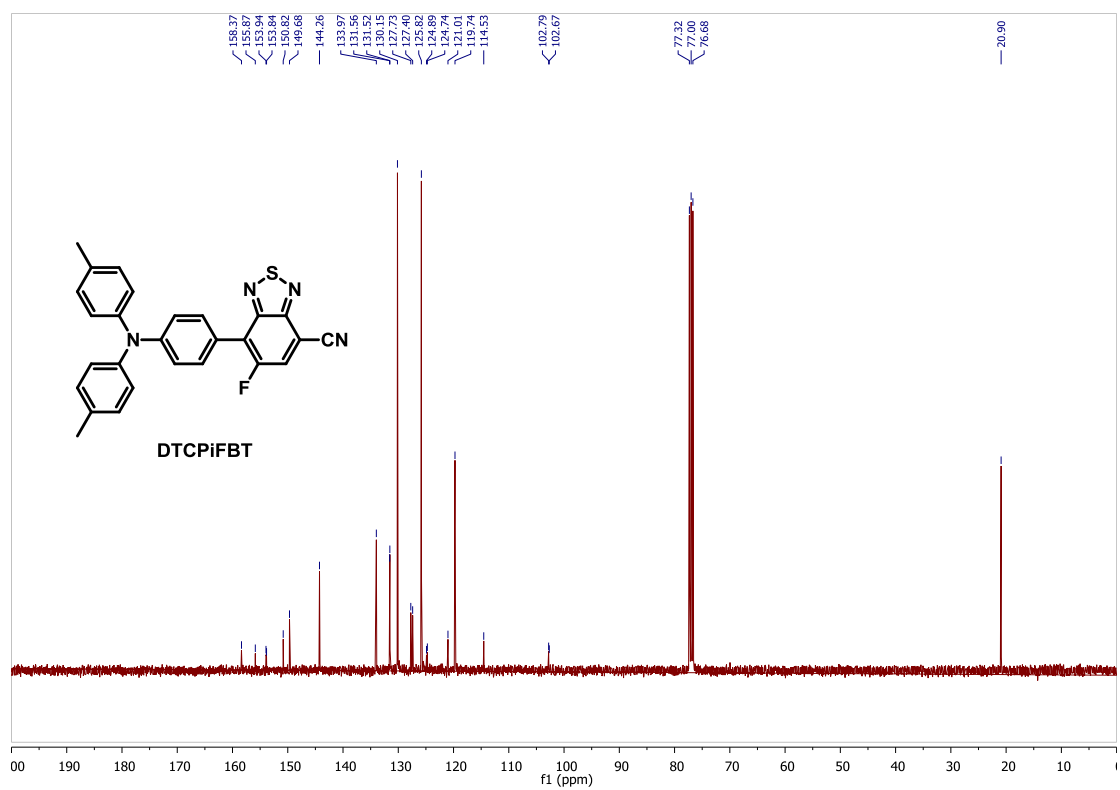


Fig. SA6. ¹³C NMR spectrum of DTCPiFBT.

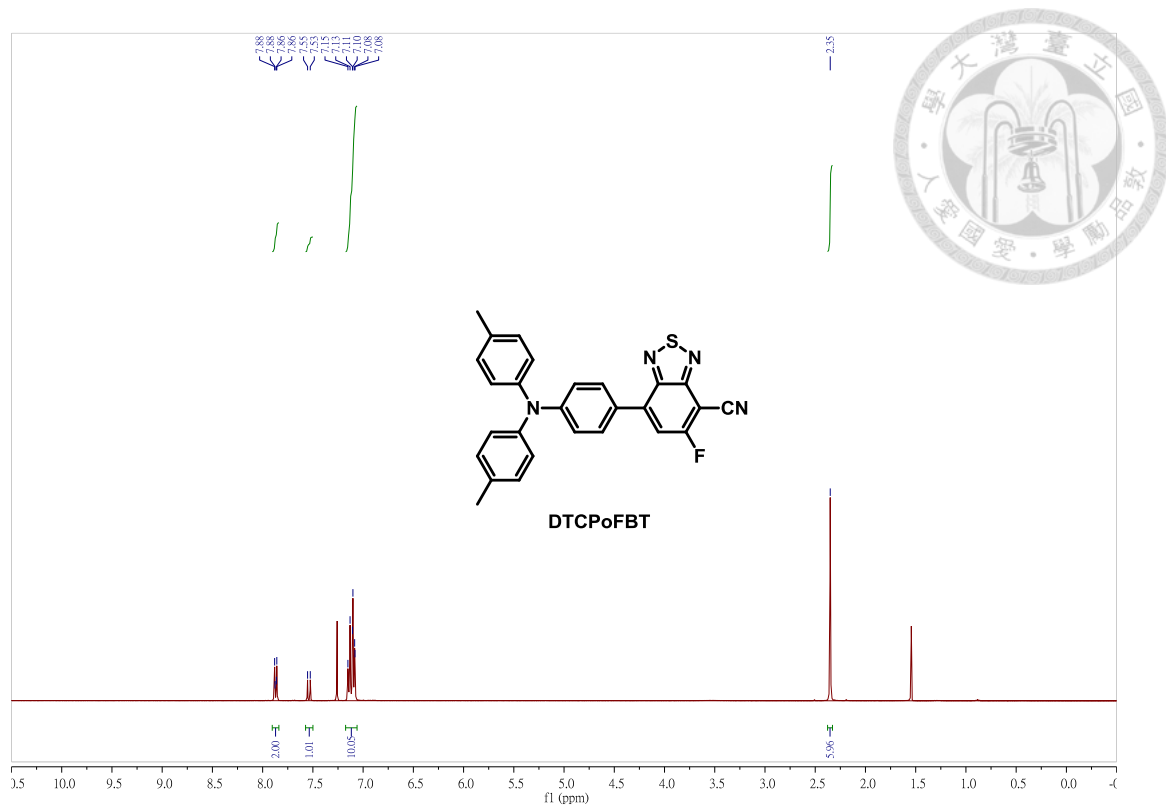


Fig. SA7. ¹H NMR spectrum of DTCPoFBT.

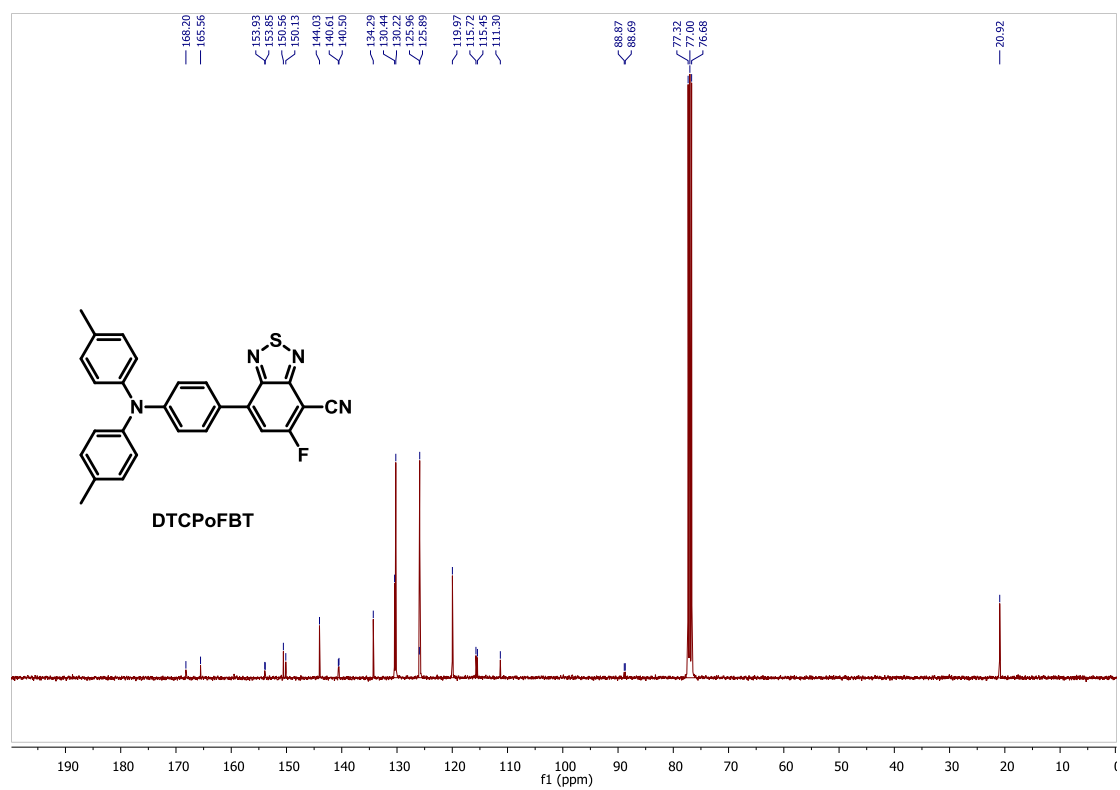


Fig. SA8. ¹³C NMR spectrum of DTCPoFBT.

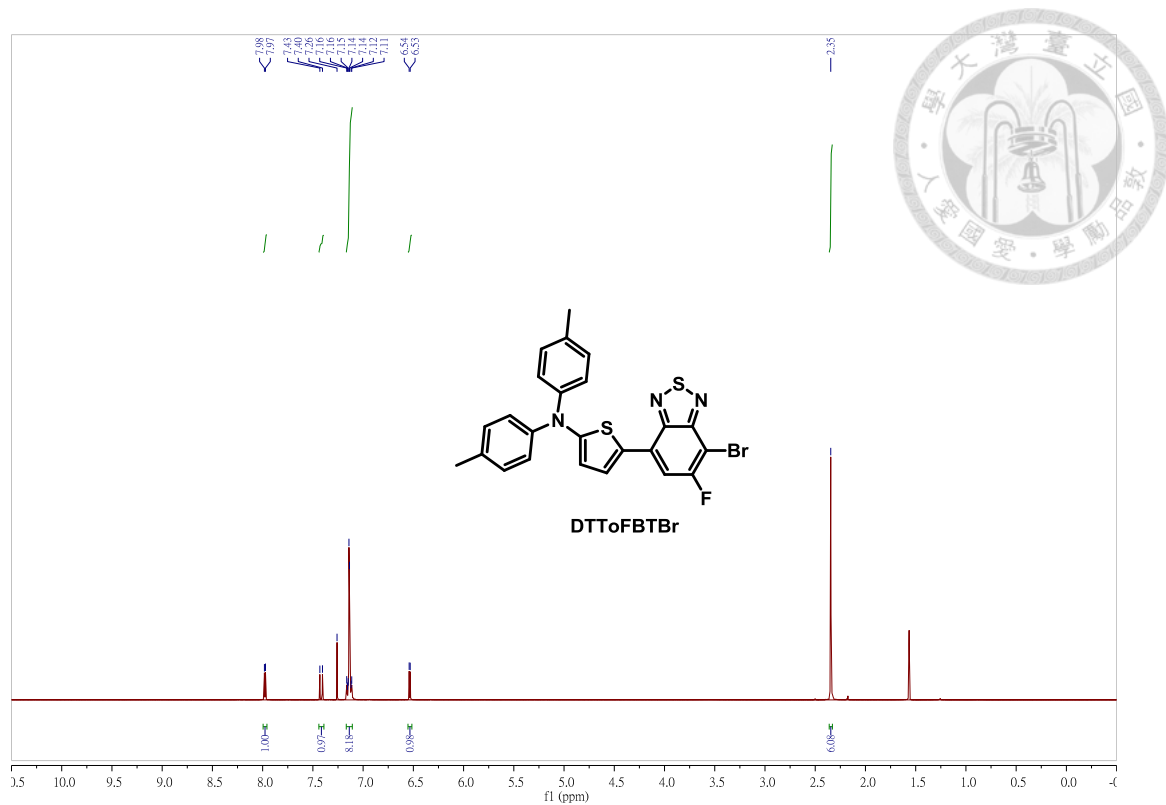


Fig. SA9. ¹H NMR spectrum of DTTToFBTBr.

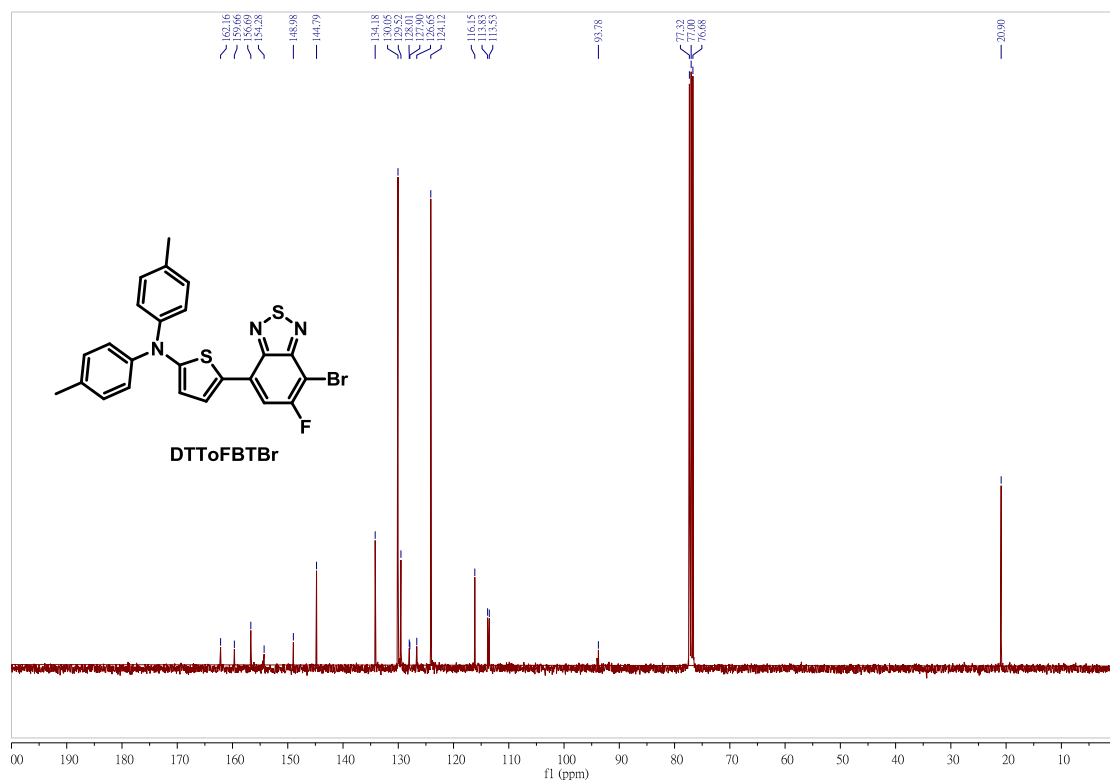


Fig. SA10. ¹³C NMR spectrum of DTTToFBTBr.

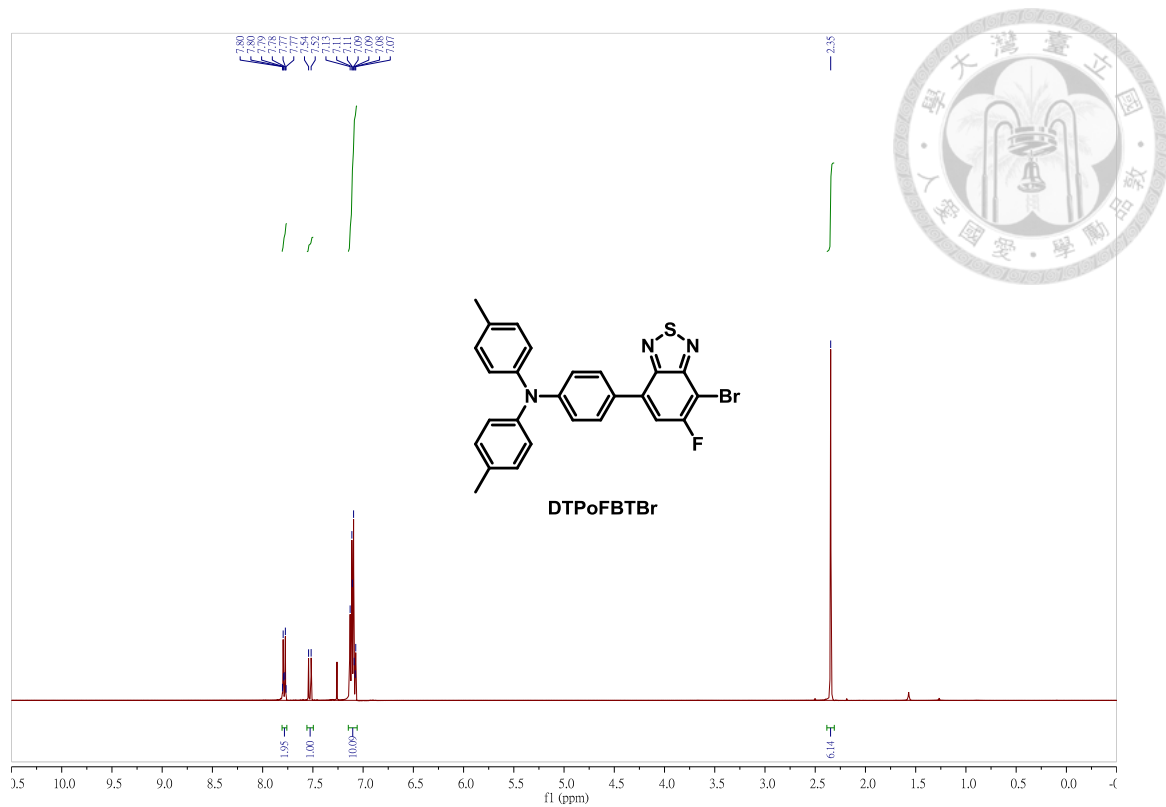


Fig. SA11. ¹H NMR spectrum of DTPoFBTBr.

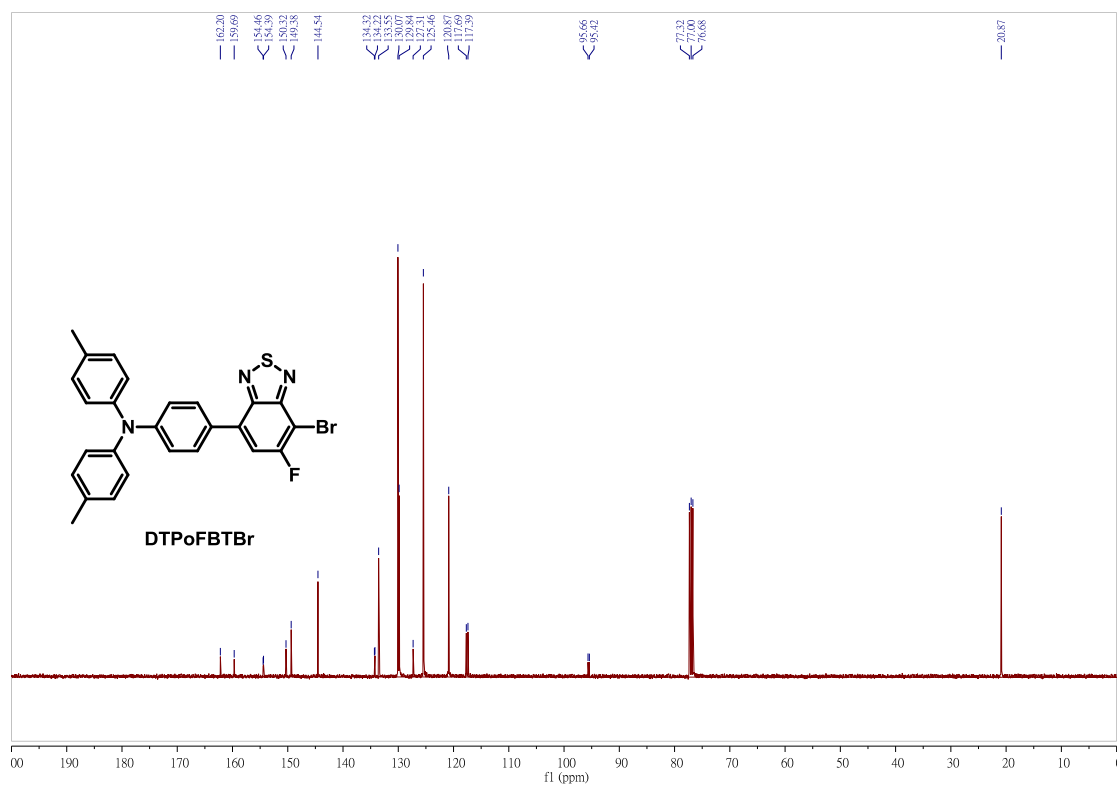


Fig. SA12. ¹³C NMR spectrum of DTPoFBTBr.

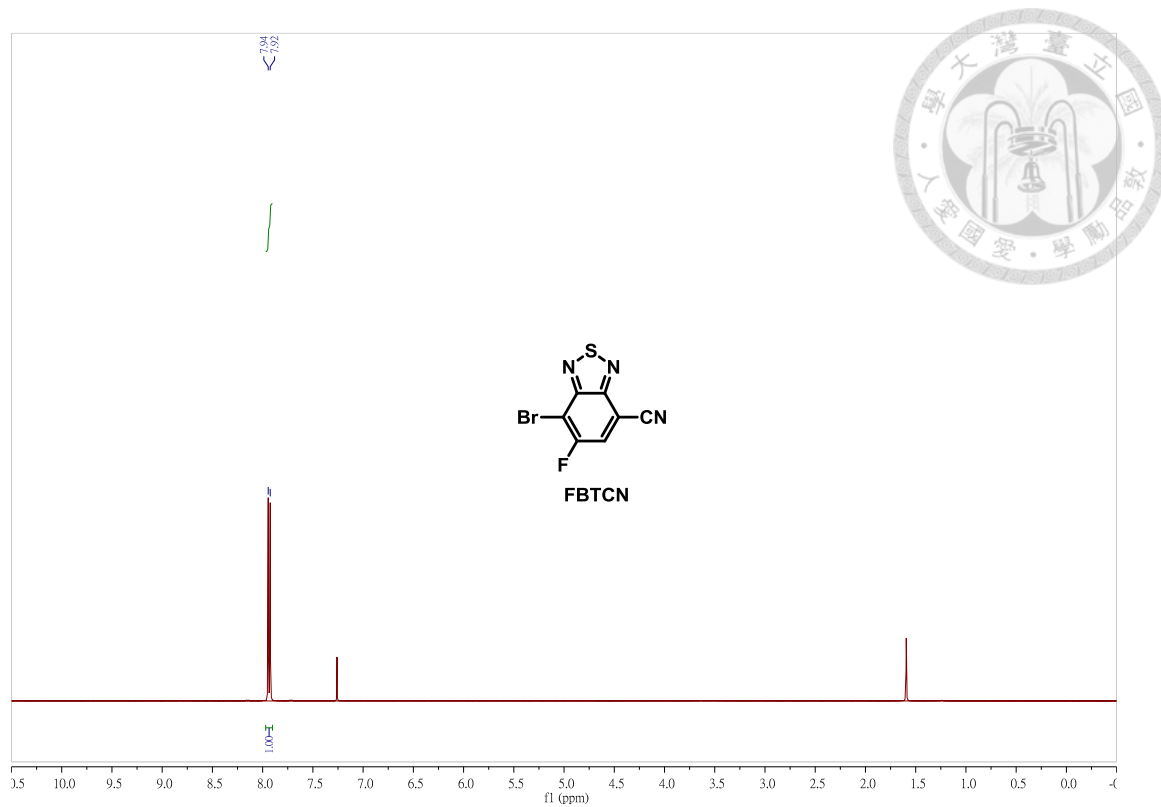


Fig. SA13. ¹H NMR spectrum of FBTCN.

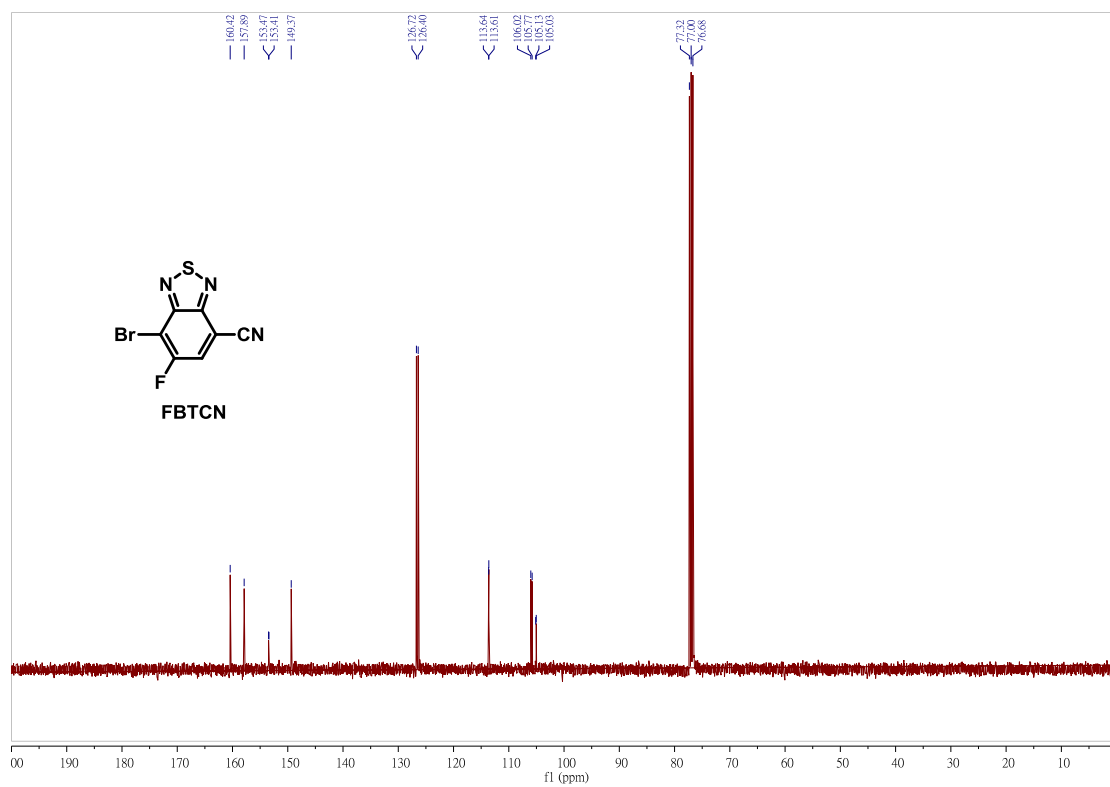


Fig. SA14. ¹³C NMR spectrum of FBTCN.



Appendix B

TGA and DSC Thermogram

Sample: CJC06-1
Size: 1.6000 mg

DSC

File: C:\...LT-DSC\10403\Operator\CJC06-1.001

Run Date: 31-Mar-2015 19:31
Instrument: 2920 MDSC V2.6A

Comment: N2

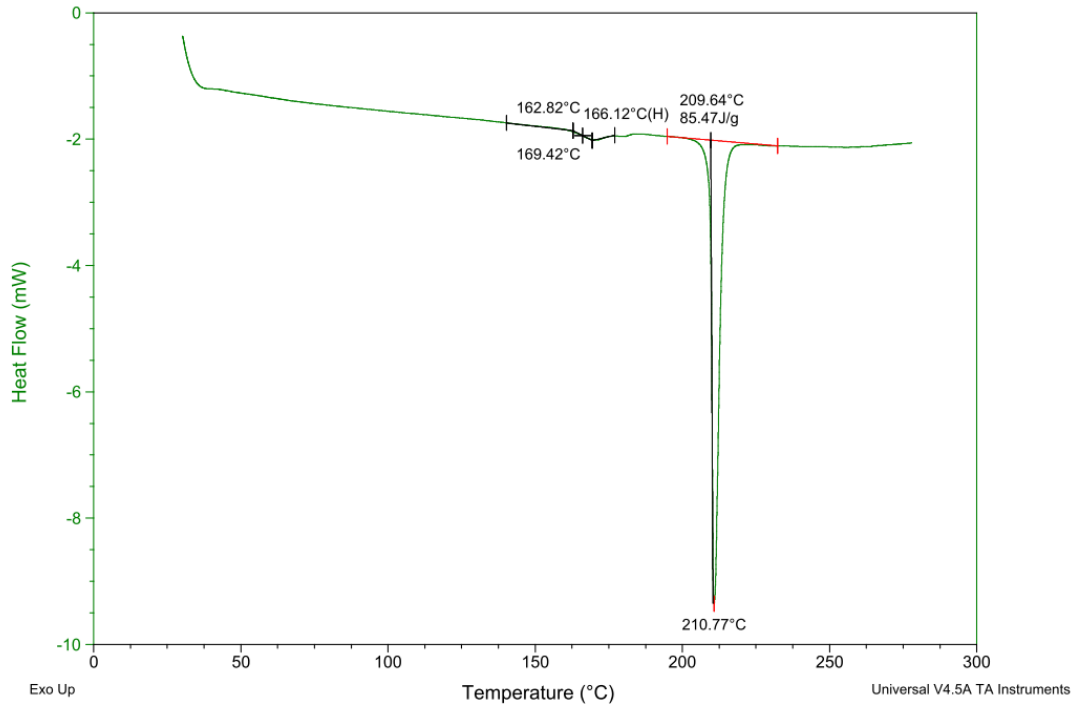


Fig. SB1. DSC thermogram of DTCTiFBT.

Sample: CJC06
Size: 4.4470 mg

TGA

File: C:\...10403\Operator\0321-31\CJC06.001

Run Date: 03-Mar-2015 21:17
Instrument: TGA Q500 V20.13 Build 39

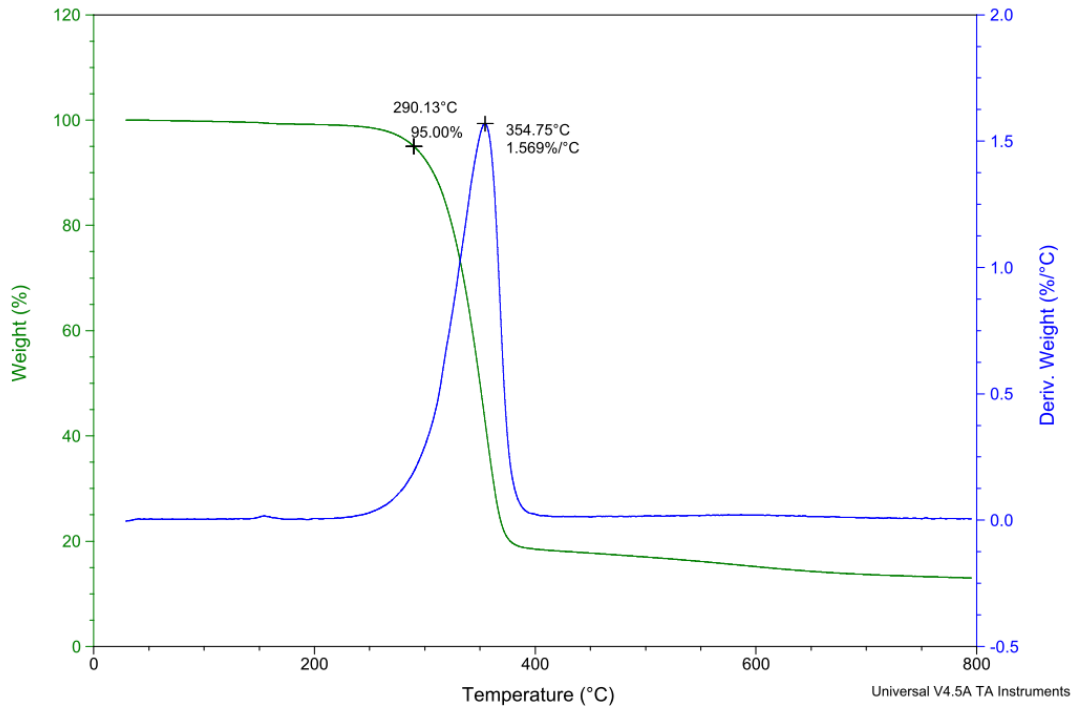


Fig. SB2. TGA thermogram of DTCTiFBT.

Sample: CJC08-1
Size: 1.0000 mg
Comment: N2

DSC

File: C:\...LT-DSC\10403\Operator\CJC08-1.001
Run Date: 31-Mar-2015 20:51
Instrument: 2920 MDSC V2.6A

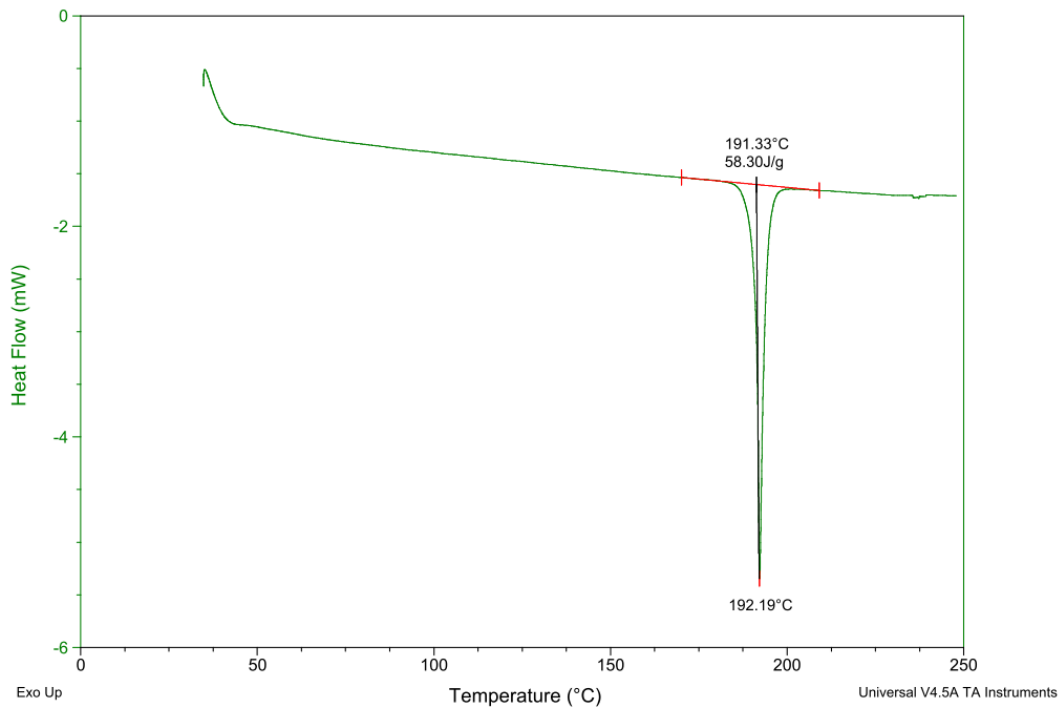


Fig. SB3. DSC thermogram of **DTCToFBT**.

Sample: CJC08
Size: 1.0600 mg

TGA

File: C:\...10403\Operator\0321-31\CJC08.001
Run Date: 03-Mar-2015 22:51
Instrument: TGA Q500 V20.13 Build 39

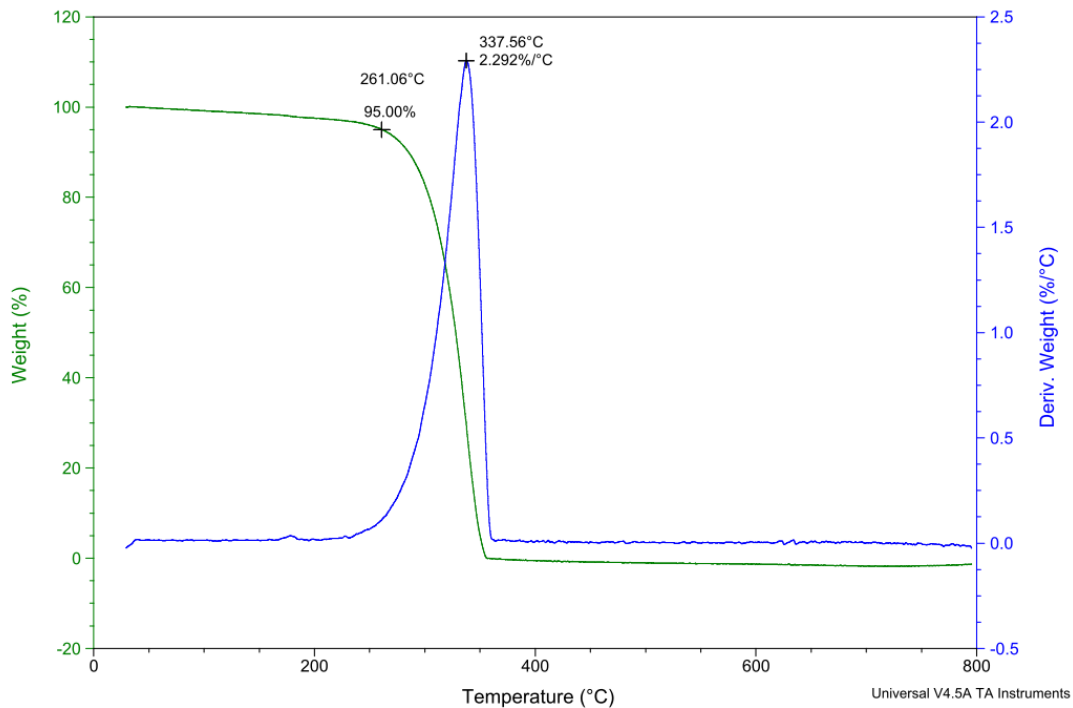


Fig. SB4. TGA thermogram of **DTCToFBT**.

Sample: CJC05-1
Size: 2.2000 mg

DSC

File: C:\...\10405\Operator\0511-20\CJC05-1.001

Run Date: 19-May-2015 15:52
Instrument: 2920 MDSC V2.6A

Comment: N2

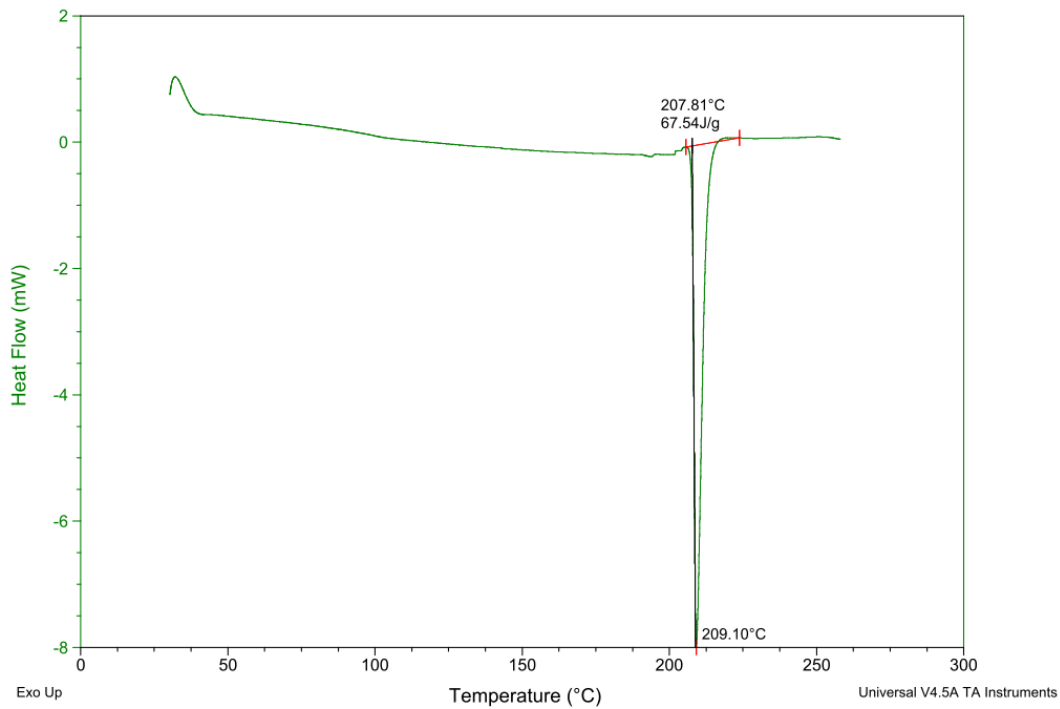


Fig. SB5. DSC thermogram of DTCPiFBT.

Sample: CJC-05
Size: 1.5530 mg

TGA

File: C:\...\10312\Operator\1221-31\CJC-05.001

Run Date: 26-Dec-2014 05:27
Instrument: TGA Q500 V20.13 Build 39

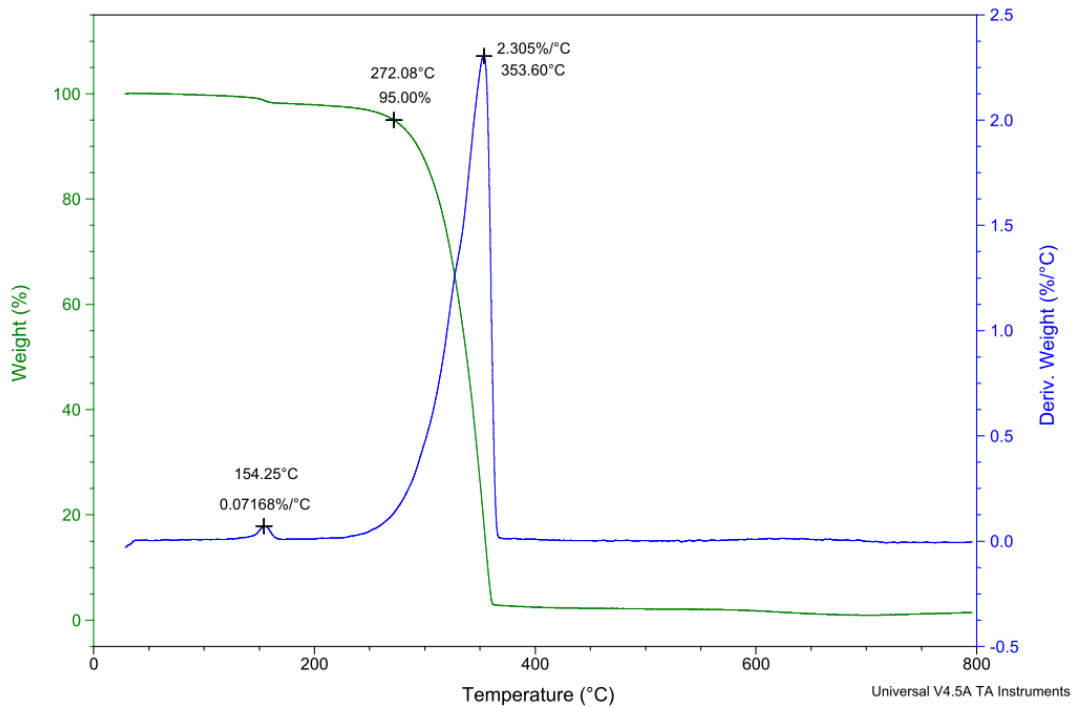


Fig. SB6. TGA thermogram of DTCPiFBT.

Sample: CJC07-1
Size: 1.5000 mg
Comment: N2

DSC

File: C:\...\10404\Operator\0421-30\CJC07-1.001
Run Date: 28-Apr-2015 16:07
Instrument: 2920 MDSC V2.6A

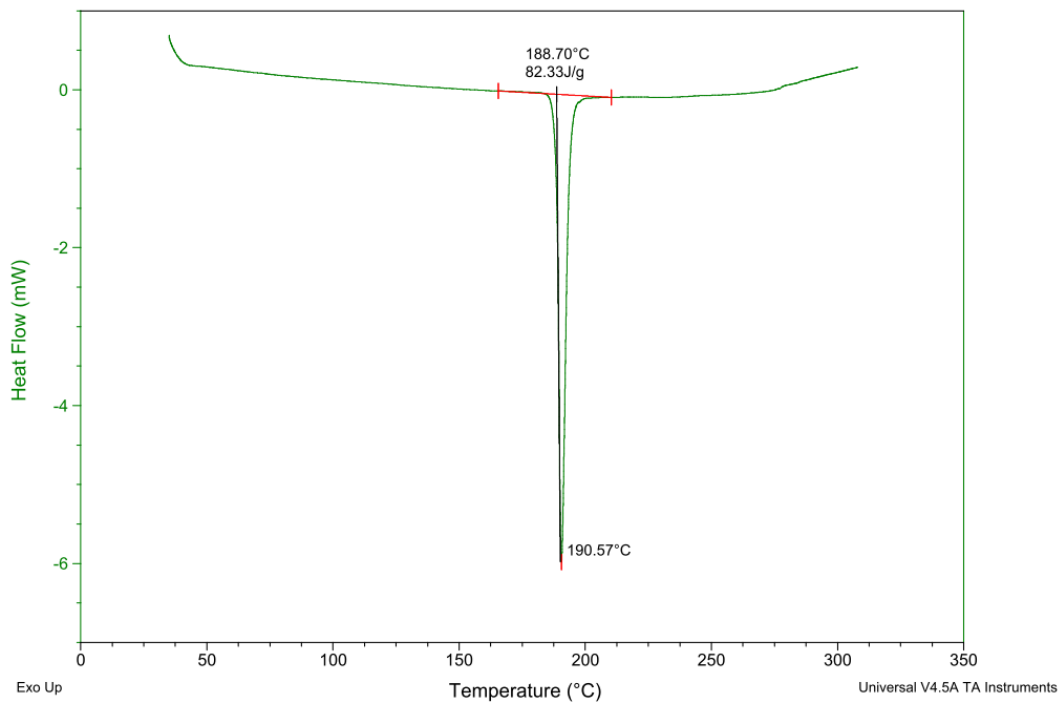


Fig. SB7. DSC thermogram of **DTCPoFBT**.

Sample: CJC07
Size: 1.2240 mg

TGA

File: C:\...\10406\Operator\0611-20\CJC07.001
Run Date: 12-Jun-2015 21:36
Instrument: TGA Q500 V20.13 Build 39

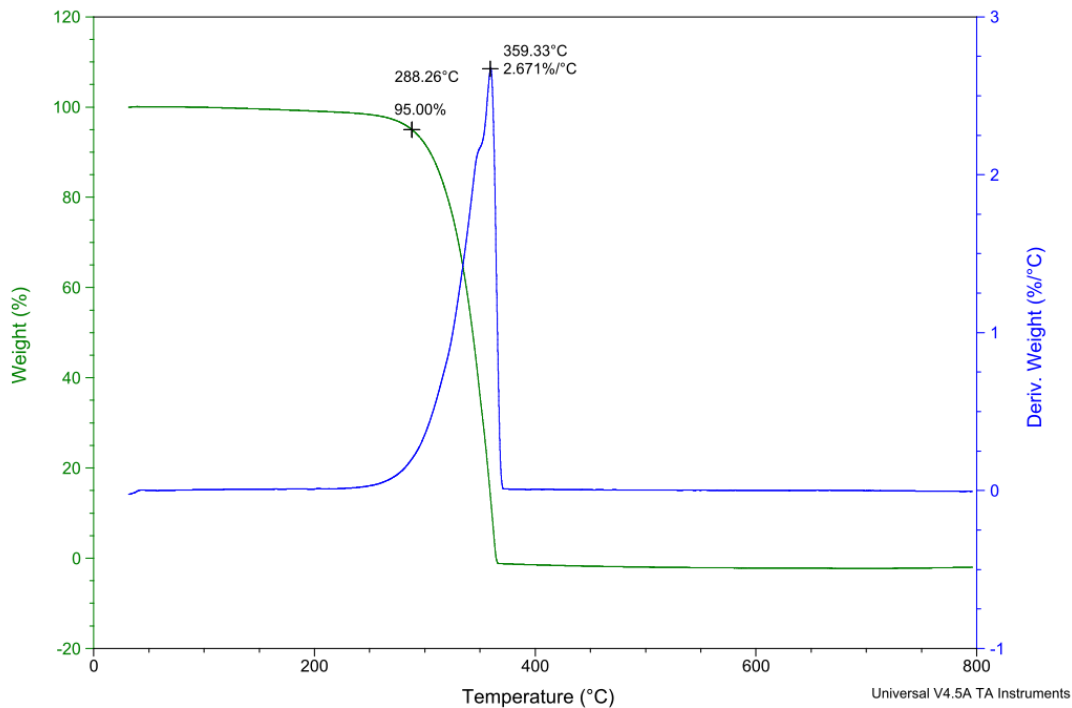


Fig. SB8. TGA thermogram of **DTCPoFBT**.



Appendix C

X-ray Crystallography Data

Table S1. Crystal data for DTCTiFBT.

Identification code	ic17327
Empirical formula	$C_{25}H_{17}FN_4S_2$
Formula weight	456.55
Temperature	200(2) K
Wavelength	1.54178 Å
Crystal system	Monoclinic
Space group	$P2_1/n$
Unit cell dimensions	$a = 16.0261(8)$ Å $\alpha = 90^\circ$ $b = 5.5990(3)$ Å $\beta = 91.242(4)^\circ$ $c = 23.3468(11)$ Å $\gamma = 90^\circ$
Volume, Z	$2094.42(18)$ Å ³ , 4
Density (calculated)	1.448 Mg/m ³
Absorption coefficient	2.557 mm ⁻¹
F(000)	944
Crystal size	0.20 x 0.20 x 0.10 mm
θ range for data collection	3.31 to 67.98°
Limiting indices	$-14 \leq h \leq 19$, $-4 \leq k \leq 6$, $-28 \leq l \leq 25$
Reflections collected	5908
Independent reflections	3774 ($R_{int} = 0.0646$)
Completeness to $\theta = 67.98^\circ$	98.8 %
Absorption correction	Semi-empirical from equivalents
Max. and min. transmission	1.00000 and 0.85649
Refinement method	Full-matrix least-squares on F^2
Data / restraints / parameters	3774 / 0 / 289
Goodness-of-fit on F^2	1.075
Final R indices [$I > 2\sigma(I)$]	$R1 = 0.0800$, $wR2 = 0.2019$
R indices (all data)	$R1 = 0.1260$, $wR2 = 0.2270$
Largest diff. peak and hole	0.546 and -0.414 eÅ ⁻³

Table S2. Crystal data for DTCPiFBT.



Identification code	ic17117
Empirical formula	$C_{28}H_{19}FN_{4.50}S$
Formula weight	469.54
Temperature	200(2) K
Wavelength	1.54178 Å
Crystal system	Monoclinic
Space group	$P2_1/n$
Unit cell dimensions	$a = 13.0581(4)$ Å $\alpha = 90^\circ$ $b = 7.1479(2)$ Å $\beta = 92.089(3)^\circ$ $c = 26.1443(7)$ Å $\gamma = 90^\circ$
Volume, Z	2438.63(12) Å ³ , 4
Density (calculated)	1.279 Mg/m ³
Absorption coefficient	1.440 mm ⁻¹
F(000)	974
Crystal size	0.20 x 0.15 x 0.10 mm
θ range for data collection	3.38 to 68.00 ^o
Limiting indices	$-15 \leq h \leq 15$, $-8 \leq k \leq 6$, $-31 \leq l \leq 20$
Reflections collected	8934
Independent reflections	4451 ($R_{int} = 0.0328$)
Completeness to $\theta = 68.00^\circ$	99.9 %
Absorption correction	Semi-empirical from equivalents
Max. and min. transmission	1.00000 and 0.97651
Refinement method	Full-matrix least-squares on F^2
Data / restraints / parameters	4451 / 0 / 310
Goodness-of-fit on F^2	1.070
Final R indices [$I > 2\sigma(I)$]	$R1 = 0.0651$, $wR2 = 0.1867$
R indices (all data)	$R1 = 0.0811$, $wR2 = 0.2058$
Largest diff. peak and hole	0.705 and -0.285 eÅ ⁻³

Table S3. Crystal data for DTCPoFBT.



Identification code	ic17313
Empirical formula	$C_{27}H_{19}FN_4S$
Formula weight	450.52
Temperature	200(2) K
Wavelength	1.54178 Å
Crystal system	Monoclinic
Space group	$P2_1/n$
Unit cell dimensions	$a = 8.5766(5)$ Å $\alpha = 90^\circ$ $b = 7.2139(4)$ Å $\beta = 96.001(5)^\circ$ $c = 36.539(2)$ Å $\gamma = 90^\circ$
Volume, Z	$2248.3(2)$ Å ³ , 4
Density (calculated)	1.331 Mg/m ³
Absorption coefficient	1.530 mm ⁻¹
F(000)	936
Crystal size	0.20 x 0.15 x 0.10 mm
θ range for data collection	4.87 to 67.99°
Limiting indices	$-9 \leq h \leq 10$, $-7 \leq k \leq 8$, $-41 \leq l \leq 43$
Reflections collected	6949
Independent reflections	4050 ($R_{int} = 0.0952$)
Completeness to $\theta = 67.99^\circ$	98.7 %
Absorption correction	Semi-empirical from equivalents
Max. and min. transmission	1.00000 and 0.94097
Refinement method	Full-matrix least-squares on F^2
Data / restraints / parameters	4050 / 0 / 298
Goodness-of-fit on F^2	0.989
Final R indices [$I > 2\sigma(I)$]	$R1 = 0.0659$, $wR2 = 0.1295$
R indices (all data)	$R1 = 0.1450$, $wR2 = 0.1741$
Largest diff. peak and hole	0.280 and -0.246 eÅ ⁻³

Table S4. Crystal data for FBTCN.



Identification code	ic17051
Empirical formula	C_7HBrFN_3S
Formula weight	258.08
Temperature	200(2) K
Wavelength	1.54178 Å
Crystal system	Monoclinic
Space group	$P2_1/n$
Unit cell dimensions	$a = 7.5848(2)$ Å $\alpha = 90^\circ$ $b = 20.3998(4)$ Å $\beta = 96.465(2)^\circ$ $c = 10.3647(2)$ Å $\gamma = 90^\circ$
Volume, Z	1593.52(6) Å ³ , 8
Density (calculated)	2.151 Mg/m ³
Absorption coefficient	9.246 mm ⁻¹
F(000)	992
Crystal size	0.25 x 0.20 x 0.15 mm
Θ range for data collection	4.33 to 67.97 ^o
Limiting indices	$-9 \leq h \leq 6, -24 \leq k \leq 14, -12 \leq l \leq 11$
Reflections collected	5567
Independent reflections	2907 ($R_{int} = 0.0470$)
Completeness to $\Theta = 67.97^\circ$	99.8 %
Absorption correction	Semi-empirical from equivalents
Max. and min. transmission	1.00000 and 0.26314
Refinement method	Full-matrix least-squares on F^2
Data / restraints / parameters	2907 / 0 / 235
Goodness-of-fit on F^2	0.921
Final R indices [$I > 2\sigma(I)$]	$R1 = 0.0457, wR2 = 0.1212$
R indices (all data)	$R1 = 0.0614, wR2 = 0.1423$
Largest diff. peak and hole	0.821 and -0.568 eÅ ⁻³